# American Journal of Science

## EARLY CENOZOIC EVOLUTION OF TOPOGRAPHY, CLIMATE, AND STABLE ISOTOPES IN PRECIPITATION IN THE NORTH AMERICAN CORDILLERA

RAN FENG*, CHRISTOPHER J. POULSEN*, MARTIN WERNER**,
C. PAGE CHAMBERLAIN***, HARI T. MIX***, and ANDREAS MULCH[§,§§,§§§]

ABSTRACT. Paleoelevation reconstructions of the North American Cordillera inferred from the oxygen ($\delta^{18}O$) and hydrogen ($\delta D$) isotope ratios of terrestrial paleoclimate proxy materials (soils, ashes, lake sediments) suggest rapid north-to-south migration of topography in the early Cenozoic (pre-49 Ma to 28 Ma). The validation of this reconstruction relies on an accurate understanding of the $\delta^{18}O_p$ and the associated regional climate change in response to the uplift of the western North America. Here we study this response using a global climate model (GCM) with explicit $\delta^{18}O_p$ diagnostics (ECHAM5-wiso) focusing on the isotopic effects of different types of precipitation, vapor mixing, recycling and moisture source and compare the response against estimates made using a Rayleigh distillation models of moist adiabatic condensation (RDM). Four experiments are performed with Eocene topography inferred from terrestrial stable isotope paleoaltimetry records to investigate how southward propagation of topography affects regional climate (temperature, precipitation and circulation pattern) and $\delta^{18}O_p$ over North America. Our experiments predict $\delta^{18}O_p$ patterns that are broadly consistent with maps of temporally binned proxy $\delta^{18}O$ and generally support an early Cenozoic north-to-south propagation of high topography in the North American Cordillera. They do not support the commonly made assumption that isotopic fractionation occurs primarily through rainout following Rayleigh distillation nor the application of modern empirical $\delta^{18}O_p$ lapse rates to past environments.

In our GCM simulations, precipitation processes and climate changes that are not captured by RDMs substantially affect $\delta^{18}O_p$. These processes include shifts in local precipitation type between convective and large-scale rain and between rain and snow; intensification of low-level vapor recycling particularly on leeward slopes; development of air mass mixing and changes in wind direction and moisture source. Each of these processes can have significant ($\geq 2‰$) influences on $\delta^{18}O_p$ that are comparable in magnitude to surface uplift of hundreds or even thousands of meters. In many regions, these processes fortuitously compensate each other, explaining the apparent agreement between ECHAM5-wiso and proxy $\delta^{18}O$ and, more broadly, between RDM estimates and observed $\delta^{18}O$-elevation relationships. In some regions, compensation is incomplete, and as a result, ECHAM5-wiso $\delta^{18}O_p$ does not agree with estimates from the RDM. In these regions, including the interior of the northern cordillera and the

* Department of Earth and Environmental Sciences, University of Michigan, Ann Arbor, Michigan 48109-1005, USA; rfeng@umich.edu
** Alfred Wegener Institute for Polar and Marine Research (AWI) Bussestrasse 24, D-27570 Bremerhaven, Germany
*** Department of Environmental Earth System Science, Stanford University, Stanford, California 94305, USA
§ Biodiversity and Climate Research Centre (BiK-F), Senckenberganlage 25, 60325 Frankfurt, Germany
§§ Goethe University Frankfurt, Institute of Geosciences, Altenhoeferallee1, 60438 Frankfurt, Germany
§§§ Senckenberg, Senckenberganlage 25, 60325 Frankfurt, Germany

**eastern flank of the southern Cordillera, moderate adjustments of paleoelevations may be in order.**

Key words: Eocene, paleoaltimetry, North American Cordillera, paleoclimate, paleoclimate modeling, oxygen isotopes, precipitation

INTRODUCTION

A wealth of geophysical, tectonic, structural and sedimentological data suggests that prior to Basin and Range extension (~23-2 Ma) crustal conditions necessary to support a high plateau existed across western North America (DeCelles, 2004; Dickinson, 2004; Chamberlain and others, 2012). When and how this plateau topography developed is an open question. Two popular tectonic models have been proposed. The first suggests that a high plateau existed early, by the Late Cretaceous, over-thickened, and then collapsed due to internal extension or frontal propagation to form a lower elevation mountainous region (see review by DeCelles, 2004). The second suggests that the plateau developed through early Cenozoic north-to-south propagation of topography as asthenosphere replaced denser mantle lithosphere due to piecemeal removal of mantle lithosphere and/or adjustment of the Farallon slab geometry (Humphreys, 1995; Forte and others, 2010; Schmandt and Humphreys, 2011). These two models call for disparate surface topography histories (Humphreys, 1995; Clark, 2007) that can potentially be distinguished through the reconstruction of past surface elevations.

To this end, Mix and others (2011) analyzed a record of over 3000 mineral samples and created temporal snapshots of the distribution of oxygen stable isotope values ($\delta^{18}O$) over western North America. These $\delta^{18}O$ snapshots show a systematic southward decrease in mineral $\delta^{18}O$ and were interpreted, following a Rayleigh condensation model, to represent rapid southward propagation of high topography (the *SWEEP* model of Chamberlain and others, 2012) from southern British Columbia to the central Great Basin of Nevada and Colorado between 50 and 28 Ma (Mix and others, 2011; Chamberlain and others, 2012).

Using mineral oxygen stable isotopic values to infer past surface elevations has become a common technique founded on modern observations that demonstrate a decrease in stable isotopic composition of precipitation ($\delta^{18}O_p$ and $\delta D_p$) with elevation at a global-average rate of approximately $-2.8\%_0 km^{-1}$ (Poage and Chamberlain, 2001). This relationship is commonly attributed to Rayleigh distillation of the heavy isotopes ($^{18}O$, D) as an ascending air parcel adiabatically cools, water vapor condenses, and precipitation forms (for example, Blisniuk and Stern, 2005). Following this theory, Rayleigh distillation models have been developed and applied to interpret stable isotope chronostratigraphies (Rowley, 2007; Rowley and Garzione, 2007). However, in some orogenic regions, Rayleigh distillation models may be inappropriate due to air parcel deflection around topography (for example, Galewsky, 2009), air mixing (for example, Gedzelman, 1988; Sherwood and Dessler, 2001) and recycling (for example, Salati and others, 1979), and the development of moist convection (for example, Risi and Vimeux, 2008; Poulsen and others, 2010). In these regions, stable isotope-elevation relationships deviate substantially from those predicted by Rayleigh distillation (Blisniuk and Stern, 2005). Examples in western North America include the Basin and Range province, which is characterized by particularly low $\delta^{18}O_p$-elevation lapse rates due to mixing and recycling of moisture from multiple sources (Lechler and Niemi, 2011), and the Sierra Nevada, which is characterized by isotopic enrichment of leeside precipitation due to orographic blocking and flow around the range (Lechler and Galewsky, 2013).

Moreover, stable isotope-elevation relationships may change as surface topography and climate evolve in concert, complicating paleoelevation reconstructions (Ehlers

and Poulsen, 2009; Poulsen and others, 2010; Poulsen and Jeffery, 2011). In the Andes of northern and central South America, for example, Cenozoic surface uplift has been demonstrated to (1) block zonal winds, leading to a shift in position of South American low-level jet to more southerly latitudes (Insel and others, 2009; Poulsen and others, 2010) and a shift in moisture source from the South Pacific Ocean to the equatorial Atlantic (Ehlers and Poulsen, 2009; Poulsen and others, 2010); (2) induce convective precipitation on the windward side flanks, enhancing isotopic fractionation through rainout (Poulsen and others, 2010; Insel and others, 2012); and (3) strengthen atmospheric subsidence and vertical mixing on the top and leeward flanks of the mountains (Poulsen and Jeffery, 2011). These effects were shown to leave strong imprints on Andean $\delta^{18}O_p$, complicating paleoelevation reconstructions. It is likely that similar phenomena affected Cenozoic $\delta^{18}O_p$ during the development of Cordilleran topography in western North America.

The purpose of this study is twofold, (i) to quantify the influence of non-Rayleigh processes on the stable isotopic composition of precipitation in and around orogenic regions and (ii) to evaluate the *SWEEP* hypothesis inferred from mineral $\delta^{18}O$ and $\delta D$. The first objective is a test of the traditional stable isotope paleoaltimetry method. If non-Rayleigh processes have a substantial influence on stable isotopic compositions, then this method is unlikely to be robust for estimating past elevations of Eocene western North America. The second objective is a test of the *SWEEP* hypothesis. Simulations of precipitation $\delta^{18}O_p$ using *SWEEP* topography should be broadly consistent with proxy $\delta^{18}O_p$. Inconsistencies between model and proxy values would bring into question the *SWEEP* reconstruction. To achieve these goals, a series of Eocene simulations have been developed using ECHAM5-wiso, a global climate model (GCM) capable of tracking water isotopologues through the hydrological cycle, to simulate the evolution of climate and $\delta^{18}O_p$ to the migration of topography described by the *SWEEP* hypothesis. These simulations are compared with both proxy $\delta^{18}O$ and estimates of $\delta^{18}O_p$ from a Rayleigh distillation model.

METHODS

*Description of the Climate Model and Boundary Conditions*

ECHAM5-wiso, a global three-dimensional atmospheric GCM with isotope-tracking capability (Werner and others, 2011), permits simulation of both early Cenozoic climate and isotopologue distribution ($H_2^{18}O$ and HDO) of vapor and precipitation over western North America. ECHAM5 has been widely used to study both past and future climate change and has been included in the Intergovernmental Panel on Climate Change (IPCC) assessment reports. Simulated temperature and precipitation means and extremes under IPCC emission scenarios fall well within the range of other GCMs, indicating reasonable model skill for projecting future climate (for example, Kharin and others, 2007). ECHAM5 also successfully simulates many aspects of modern North American climate, including the distribution of precipitation over western North America (Salathé, 2006; Cook and others, 2008). In comparison to other GCMs, ECHAM5 produces a more realistic simulation of the Aleutian low and the storm track over the Pacific Northwest (Salathé, 2006). ECHAM5, coupled to the ocean model MPI-OM, also does a better job of simulating zonal precipitation gradients across central and western North America than many other GCMs (Cook and others, 2008). Finally, in comparison to many GCMs, ECHAM5_MPI-OM simulates an Eocene climate with a lower equator-to-pole temperature gradient and ice-free Arctic at low $CO_2$ level of 560 ppmv (Heinemann and others, 2009).

In ECHAM5-wiso, water isotopologues are treated as independent tracers that undergo equilibrium and kinetic fractionation during phase transitions in the atmosphere. Vapor fluxes from the sea surface and lakes undergo non-equilibrium fraction-

ation as a function of temperature, seawater $\delta^{18}O$ ($\delta^{18}O_{sw}$), relative humidity and $\delta^{18}O$ of vapor at the bottom of the atmosphere. Vapor fluxes from the land surface are not fractionated (Hoffmann and others, 1998), since root uptake and transpiration have minimal effect on the isotopic composition (Zimmermann and others, 1967). Seawater $\delta^{18}O$ ($\delta^{18}O_{sw}$) is prescribed at each grid cell as described below. Lake water $\delta^{18}O$ is set to a constant value of 0.5 permil. Surface runoff and drainage are based on a single bucket scheme (Roeckner and others, 2003). Water isotopologues that infiltrate the surface are treated as passive tracers (Hoffmann and others, 1998). The $\delta^{18}O$ of runoff is assumed to be the same as soil water. The water isotope-tracking module of ECHAM has been used to investigate modern (Hoffmann and others, 1998; Werner and others, 2011) and past hydrological cycles (Hoffmann and others, 2000). For North America, the simulations have been shown to be in good agreement with observed $\delta^{18}O_p$ from the Global Network of Isotopes in Precipitation (GNIP) and vapor $\delta D$ by Scanning Imaging Absorption Spectrometer for Atmospheric Cartography (SCIAMACHY) (Frankenberg and others, 2009) (figs. 1 and 10 in the paper by Werner and others, 2011).

ECHAM5-wiso can be coupled to a 50-m mixed-layer ocean model with prescribed ocean heat flux (Roeckner and others, 2003). However, in the absence of knowledge about Eocene ocean heat fluxes, monthly-varying sea-surface temperatures (SSTs) were prescribed in all experiments. The Eocene SST dataset was calculated (i) using ECHAM5 with a mixed-layer ocean model and modern ocean heat fluxes to estimate the zonal distribution of SST, and (ii) then modifying the resulting SST distribution to replicate the Eocene meridional temperature gradient reconstructed from multiple proxies (fig. 1C). As a result of this procedure, the SST distribution has zonal features reminiscent of modern including a west-east equatorial temperature gradient, poleward warming in the vicinity of subtropical western boundaries, and equator-ward cooling along subtropical eastern boundaries (fig. 1A), yet a meridional gradient that is appropriate for the Eocene (fig. 1C).

ECHAM5-wiso requires the input of seawater $\delta^{18}O$ values. We estimated these values from a lower resolution (spectral T31, ~3.75° in latitude and longitude) Eocene simulation using a coupled ocean-atmosphere model with isotope-tracking capability (GENMOM, Zhou and others, 2008). Our Eocene simulation was run with boundary conditions (that is geometry, topography, $CO_2$) similar to those used in our ECHAM5-wiso experiments, and a flat ocean with a depth of 5600 m. The simulation was initialized with uniform $\delta^{18}O_{sw}$ of $-1.2$ permil, the average $\delta^{18}O_{sw}$ in an ice-free world, and was integrated for 2020 model years, until the time rates of change of upper-ocean temperature and salinity were $<0.1$ °C/100yrs and 0.1 ‰/100yrs. Northward of 75° N, the $\delta^{18}O_{sw}$ simulated by GENMOM is less than $-7$ permil, due to insufficient seawater exchange across the Bering Straight in this low resolution simulation (Zhou and others, 2008). To correct for this bias, we set the minimum Arctic $\delta^{18}O_{sw}$ to $-4$ permil, about the value of the modern Arctic (Clementz and Sewall, 2011). The average of the last 40 years of $\delta^{18}O_{sw}$ and $\delta D$ from the GENMOM Eocene simulation were used as boundary conditions in the ECHAM5-wiso simulations. The meridional $\delta^{18}O_{sw}$ gradient is roughly similar to the modern gradient with a low gradient at low latitudes and a higher gradient (0.06‰ latitude$^{-1}$) at middle to high latitudes (between 30° N to 70° N and 30° S to 60° S).

In all experiments, ECHAM5-wiso is configured with 19 vertical levels and a spectral triangular truncation of 106 horizontal waves (~100 km horizontal grid spacing). In comparison to most paleoclimate simulations, with horizontal grid spacing of 200 to 300 km, our resolution is finer in order to better capture orographic processes. We use the Eocene paleogeography and paleotopography from Bice and others (2000) but modify the geography over western North America to include foreland basins with mean elevations of 500 m and interior lakes. Both basins and lakes
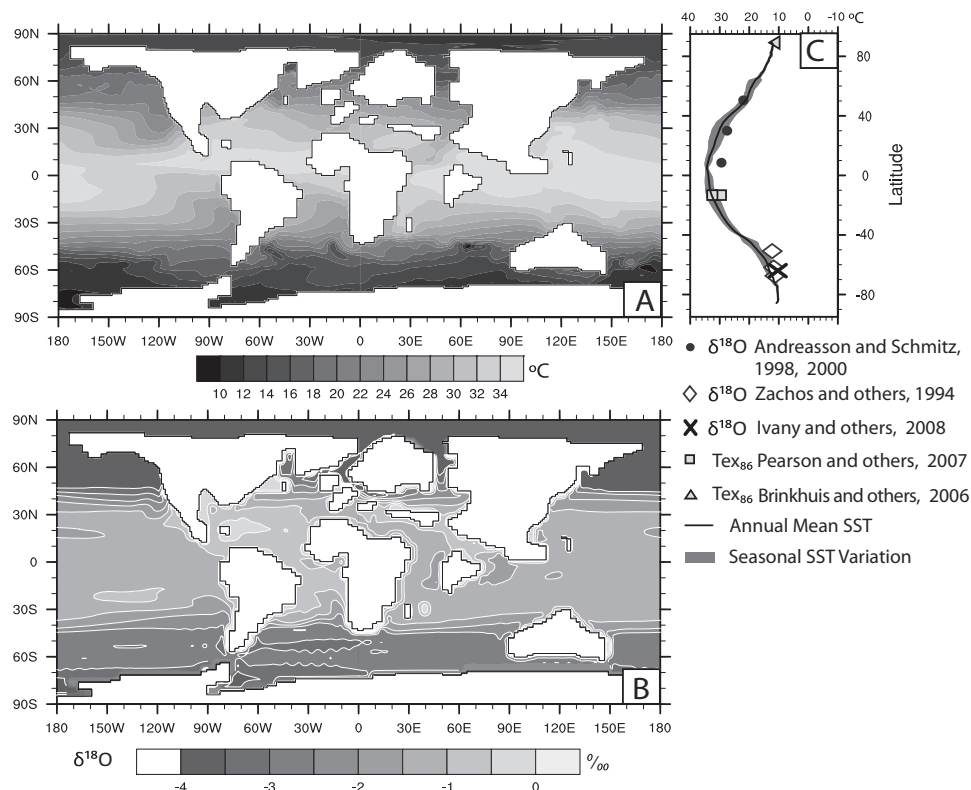
Fig. 1. Annual mean Eocene (A) sea surface temperature (SST, °C), (B) seawater $\delta^{18}O$ ($\delta^{18}O_{sw}$, ‰) and (C) meridional SST gradient (line) and its seasonal variation (gray shading) versus proxy reconstructions (markers). SST and $\delta^{18}O_{sw}$ are fixed boundary conditions in this study.

are inferred from the stratigraphic analysis of Eocene sedimentary successions by Dickinson and others (1988).

We have developed a series of experiments to investigate the influence of Cenozoic paleotopographic evolution on regional $\delta^{18}O_p$ and climate. The only parameter that varies between experiments is the land-surface topography; all other boundary conditions remain the same between experiments (table 1). Four scenarios are simulated including a control case with no significant highlands (CNTL) and a series of three cases that portray progressive Cenozoic uplift of the North American Cordillera from north to south following the reconstructions of Mix and others (2011). These cases are referred to as northern highlands (NHL), central highlands (CHL), and southern highlands (SHL) (fig. 2). All experiments were run until the time rate of change of the global surface temperature was $\leq 0.01°C\,yr^{-1}$. The simulations were then integrated an additional ten years. All results in this study are reported as averages of the final ten years.

### Rayleigh Distillation Model of Adiabatic Condensation (RDM)

We have constructed a Rayleigh distillation model of adiabatic condensation (RDM), similar in concept to that outlined in Rowley and Garzione (2007), as a diagnostic tool to (i) evaluate the extent to which local $\delta^{18}O_p$ in our ECHAM5-wiso simulations can be described by Rayleigh distillation and (ii) quantify the biases

Table 1

*Boundary conditions for our ECHAM5-wiso Eocene experiments*

| Parameter | Model input |
| --- | --- |
| Topography | 55 Ma (Bice and others, 2001) |
| Vegetation | The Eocene vegetation distribution is based on Sewall and others (2000). Surface parameters including albedo, roughness length, field capacity of soil, and forest ratio, are prescribed according to Hagemann (2002) based upon vegetation type. |
| $p$N$_2$O and $p$CH$_4$ | 306 ppb and 1.65 ppm (modern values) |
| $p$CO$_2$ | 1120 ppm (Beerling and others, 2011) |
| Sea ice and glacial ice | None |
| Sea water $\delta^{18}$O ($\delta^{18}$O$_{sw}$) | Prescribed from GENMOM Eocene simulation |
| SST | Prescribed SSTs with mean and meridional distribution to fit Eocene proxy |

associated with assuming a fixed moisture source in paleoaltimetry estimates. The RDM, described in detail in Appendix A, is a one-dimensional (altitude dependent) model that tracks the isotopic composition of a single near-surface air parcel as it ascends, becomes saturated, and condenses. The model assumes that as an air parcel attains saturation, the resulting condensate is immediately removed from the system.

The RDM requires knowledge of the initial vapor temperature ($T_s$), specific humidity ($q_s$), and $\delta^{18}$O$_v$ of the ascending air mass. In applications of RDMs for paleoaltimetry purposes, $\delta^{18}$O$_v$ is often prescribed from proxy data assuming a known moisture source. For example, in their use of an RDM to estimate paleoelevations, Mix and others (2011) used mineral $\delta^{18}$O from an Eocene coastal site based on the assumption that, as today, these sites received most of their moisture from the western Pacific Ocean.

In our application of the RDM, we run two types of experiments: those with *fixed-moisture* sources and those with *GCM-moisture* sources. *Fixed-moisture* source experiments are intended to quantify the bias introduced by a uniform western Pacific source and a constant initial $\delta^{18}$O$_v$ (inferred from mineral $\delta^{18}$O$_p$). In these experiments, initial vapor temperature and specific humidity are specified from GCM mean-annual surface temperature and low-level (1000 hPa) specific humidity from the western side of each highland (values are shown in fig. 3). In our *GCM-moisture* source experiments, initial vapor $\delta^{18}$O$_p$, in addition to temperature and specific humidity, are specified from mean-annual GCM output. We use the RDM to track air masses from both the western and eastern sides of the range. Though it is typically assumed that all moisture sources from the west, our GCM simulations and simulations by Sewall and Sloan (2006) indicate that this is not the case. Initial $T_s$, $q_s$ and $\delta^{18}$O$_v$ values of *GCM-moisture* sources (GCM-derived $\delta^{18}$O$_v$ and moisture source) for each side of the highlands (dash line square) and the $\delta^{18}$O$_v$ values of *fixed-moisture* sources (solid line square) are shown in figures 3A–3C.

The RDM describes an open isotopic system, in which the condensation is continuously removed. Yet, in our GCM simulations, recycling through evaporation of surface water can account for up to ~70 percent to 76 percent of precipitation on the leeside of the Cordillera. To account for this process, we have developed a modified RDM that incorporates vapor recycling. At each time step, a portion of any condensate, equal to the condensate mass times the recycling potential, is added back to the air mass. The recycling potential is defined as the local ratio of surface evaporation to
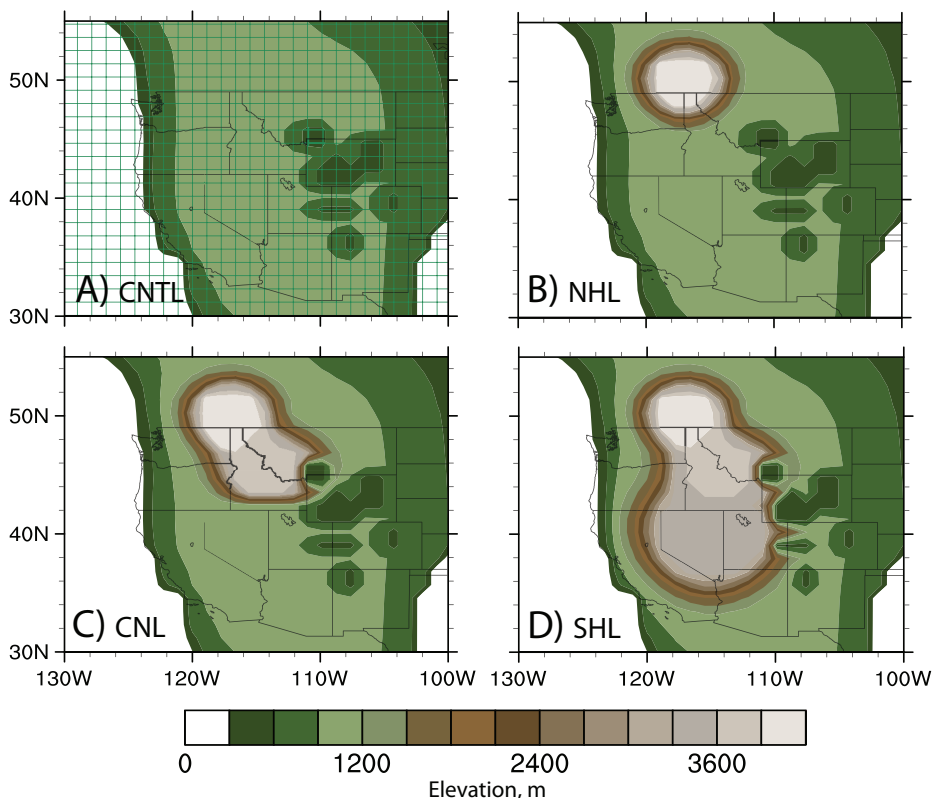
Fig. 2. Topography of western North America for the (A) control (CNTL), (B) northern highland (NHL), (C) central highland (CHL) and (D) southern highland (SHL) experiments. NHL, CHL, and SHL are modified after Mix and others (2011) and represent the southern propagation of an Eocene highland through the early Cenozoic. The grid lines in (A) represent the computational grid used in our ECHAM5-wiso experiments. U.S. state borders are shown to simplify the referencing of sample locations. The borders have been modified to account for Neogene Basin and Range extension by narrowing Nevada by ~2° longitude.

precipitation from GCM output averaged over the leeside of the mountain and neglects vapor integrated through mixing and transport aloft. The vapor temperature and isotopic ratio are unchanged by assuming isothermal expansion and that recycled vapor has the same isotopic ratio as existing vapor (details see Appendix B).

### Analysis of $\delta^{18}O_l$ Mixing

In contrast to the scenario depicted in RDMs, an air parcel is not isolated and may interact with its environment through mixing, which can change both its isotopic composition and humidity. At the local scale, mixing between a parcel and its environment happens primarily through turbulence. On regional and continental scales, mixing can also occur through large-scale circulation (Pierrehumbert and Yang, 1993). This type of mixing includes vapor entrainment through moist convection and lateral mixing of dry air and moist plumes through advection. The former is of primary importance in the tropics (Pierrehumbert and Yang, 1993), while the latter is most important in subtropical regions (Pierrehumbert, 1998). As evidenced by global observations of mid-troposphere δD (Worden and others, 2007) and demonstrated in GCM simulations (Poulsen and Jeffery, 2011), large-scale mixing through subsidence
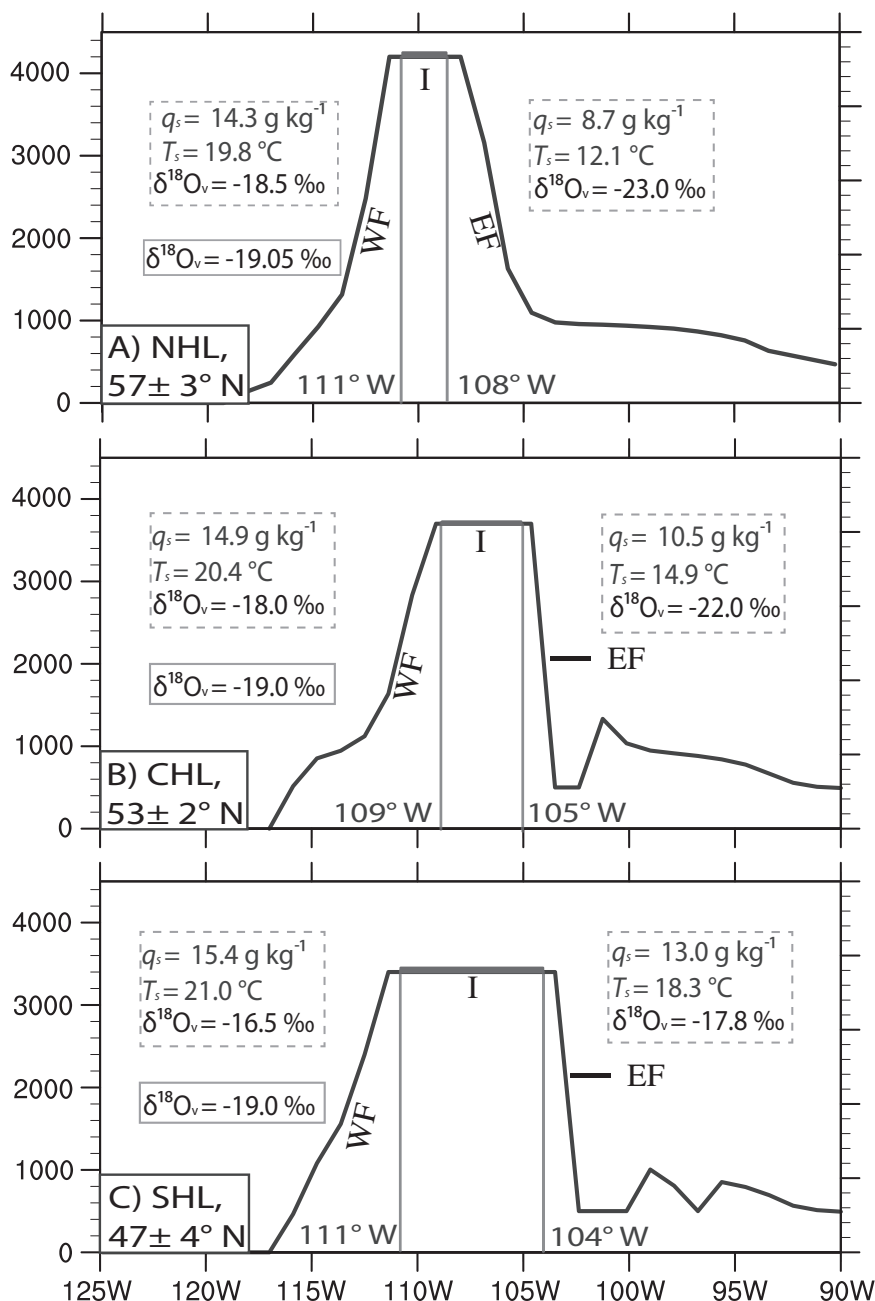
Fig. 3. Topographic cross-section across northern (NHL), central (CHL) and southern (SHL) high-lands. The different topographic regimes (western flank, WF; eastern flank, EF; and interior, I) discussed in the text are labeled. The specific humidity ($q_s$), temperature ($T_s$) and $^{18}O$ composition of vapor ($\delta^{18}O_v$) of *GCM*-moisture source (dashed box) and $\delta^{18}O_v$ (solid box) are show. The $q_s$ and $T_s$ of *fixed*-moisture source are the same as the *GCM*-moisture source at the western flank (dashed box at the western flank).

and convection can significantly affect the isotopic composition of vapor. Mixing can change vapor isotopic composition by changing (i) the isotopic composition of the air parcel; (ii) the fractionation temperature of condensate; and (iii) the relative humidity, and thus condensation potential, of the air parcel (for example, Sherwood and Dessler, 2001).

To estimate the effect of vapor mixing on the $\delta^{18}O_p$, we calculate the $\delta^{18}O$ of equilibrium condensate ($\delta^{18}O_c$) from the advection potential of $\delta^{18}O_v$ using the GCM output of $\delta^{18}O_v$ and three-dimensional wind velocities. The temporal change of $\delta^{18}O_c$ due to flow in the s-direction (either zonal, meridional or vertical direction), $\dfrac{\partial \delta^{18}O_c}{\partial t}$, can be approximated using the advection equation:

$$\frac{\partial \delta^{18}O_c}{\partial t} \sim - V_s \frac{\partial \delta^{18}O_c}{\partial s} \tag{1}$$

where $\dfrac{\partial \delta^{18}O_c}{\partial s}$ and $V_s$ are the $\delta^{18}O_c$ gradient and flow velocity.

The $\dfrac{\partial \delta^{18}O_c}{\partial s}$ is estimated by assuming immediate condensation of advected vapor:

$$\delta^{18}O_c \approx \delta^{18}O_v + 1000 \ln \alpha \tag{2}$$

where $\alpha$ is the fractionation factor. $1000\ln\alpha$ describes isotopic fractionation due to condensation and is expanded as in Majoube (1971):

$$1000 \ln \alpha = -7.685 + \frac{6.7123 \times 10^3}{T} - \frac{1.6664 \times 10^3}{T^2} + \frac{0.35041 \times 10^9}{T^3}. \tag{3}$$

Computing the $\delta^{18}O$ gradient on both side of equation (2) gives:

$$\frac{\partial \delta^{18}O_c}{\partial s} = \frac{\partial \delta^{18}O_v}{\partial s} + \frac{\partial T}{\partial s}\left(- \frac{6.7123 \times 10^3}{T^2} + \frac{3.3328 \times 10^6}{T^3} - \frac{1.05123 \times 10^9}{T^4}\right), \tag{4}$$

where $\dfrac{\partial T}{\partial s}$ is the temperature gradient along the s-direction. Calculating the inner dot product of the velocity and gradients in the s-direction on both sides of equation (4) yields:

$$V_s\frac{\partial \delta^{18}O_c}{\partial s} = V_s\frac{\partial \delta^{18}O_v}{\partial s} + V_s\frac{\partial T}{\partial s}\left(- \frac{6.7123 \times 10^3}{T^2} + \frac{3.3328 \times 10^6}{T^3} - \frac{1.05123 \times 10^9}{T^4}\right). \tag{5}$$

$V_s$, T and $\delta^{18}O_v$ are then rewritten as the sum of the annual mean and its perturbation, following the form $x = \bar{x} + x'$. Expanding the right-hand side, neglecting the high-order term $\left(\dfrac{\overline{T'^2}}{\overline{T}^2}, \dfrac{\overline{T'^4}}{\overline{T}^4} \text{ and } (\delta^{18}O_v)'\right)$, and taking the annual average yields:

$$\overline{V_s\frac{\partial \delta^{18}O_c}{\partial s}} \approx \overline{V_s}\,\overline{\frac{\partial \delta^{18}O_v}{\partial s}} + \left(\overline{V_s}\frac{\partial \bar{T}}{\partial s} + \overline{V'_s\frac{\partial T'}{\partial s}}\right)\left[- \frac{6.7123 \times 10^3}{\bar{T}^2} + \frac{3.3328 \times 10^6}{\bar{T}^3}\right.$$
$$\left. - \frac{1.05123 \times 10^9}{\bar{T}^4}\right]. \tag{6}$$

The mean annual advection of $\delta^{18}O_c$ is determined by the mean-annual advection of $\delta^{18}O_v$ and $T$, and the annual average of sub-annual scale advection of $T'$. As a first order approximation, this part of advection is estimated with monthly climatology. Advection terms are estimated using center differencing and are averaged to the mid-point of each grid cell in the vertical direction.

The $\dfrac{\partial \delta^{18}O_c}{\partial t}$ is then estimated using equation (1). The calculation assumes that vapor into a grid cell immediately mixes with the existing vapor following the equilibrium liquid condensation. This approximation has several sources of potential error. First, not all of the vapor into a grid cell will condense to form precipitation. Second, condensate may form solid precipitation (snow, hail), particularly in updrafts, which undergoes kinetic fractionation and diffusive processes, leading to a smaller fractionation factor. As a result of these errors, our estimate of $\delta^{18}O_c$ changes due to advection likely represent an upper bound.

### Analysis of Moisture Source through Back Trajectory

To locate the source of orographic moisture in our experiments, we calculate horizontal back trajectories of high-humidity, low-level air parcels originating from positions on the highlands. Back trajectories are calculated from 10-year daily climatologies of humidity-weighted (averaged between 1000 and 850 hPa) winds from our ECHAM5-wiso experiments. Each back trajectory is calculated for 7 prior days with a 1-hour time step. Wind speeds at each time step are calculated by linearly interpolating between daily values. The use of daily climatologies filters the velocity field, eliminating the influence of transient eddies. Additional details about our back trajectory method are described in Appendix C.

For the NHL, CHL, and SHL cases, back trajectories are performed for the following locations on the western flank and eastern flank: 57° N, 125° W and 115° W (NHL case); 53° N, 122° W and 102° W (CHL case); and 47° N, 125° W and 102° W (SHL case). For comparison, back trajectories from the same locations are also calculated for the CNTL case. For each location, 365 back trajectories are calculated beginning on the 1st of January and extending through the 31st of December. Air parcel relative humidity is also recorded along the trajectory path. Trajectories are only reported for air parcels at starting location with relative humidity ≥60 percent.

### RESULTS

### Simulated Early Eocene Temperature of Western North America

Mean annual temperature (MAT) in the CNTL experiment is largely zonal over North America ranging from a minimum of 9.2 °C at high latitudes to a maximum of 27.5 °C over southwestern North America (fig. 4A). The simulated latitudinal MAT gradient is ~0.5 °C latitude$^{-1}$ between 40° N and 70° N at 100° W, slightly higher than the Early Eocene *equable climate* gradient reconstructed from paleofloras (~0.4 °C latitude$^{-1}$, Greenwood and Wing, 1995). The cold month mean temperature has a similar zonal distribution with minimum of 2.6 °C and maximum of 15 °C. The inclusion of highlands disrupts the zonal distribution of MATs, depressing temperatures in their vicinity (figs. 4B-D). The minimum MAT of all three sensitivity experiments drops to −7.6 °C on the highland top with sharp zonal gradients on the western and eastern flanks with average magnitudes of ~2.7 and ~1.8 °C longitude$^{-1}$. The smaller MAT gradient along the eastern flanks is partly due to the development with highlands of both stationary and mountain gravity waves, which promote cold air mass intrusion from the north and from the mountain top.

In general, surface temperatures in our CNTL experiment agree with western North American paleotemperature based on early Eocene floras (>49 Ma) from lower
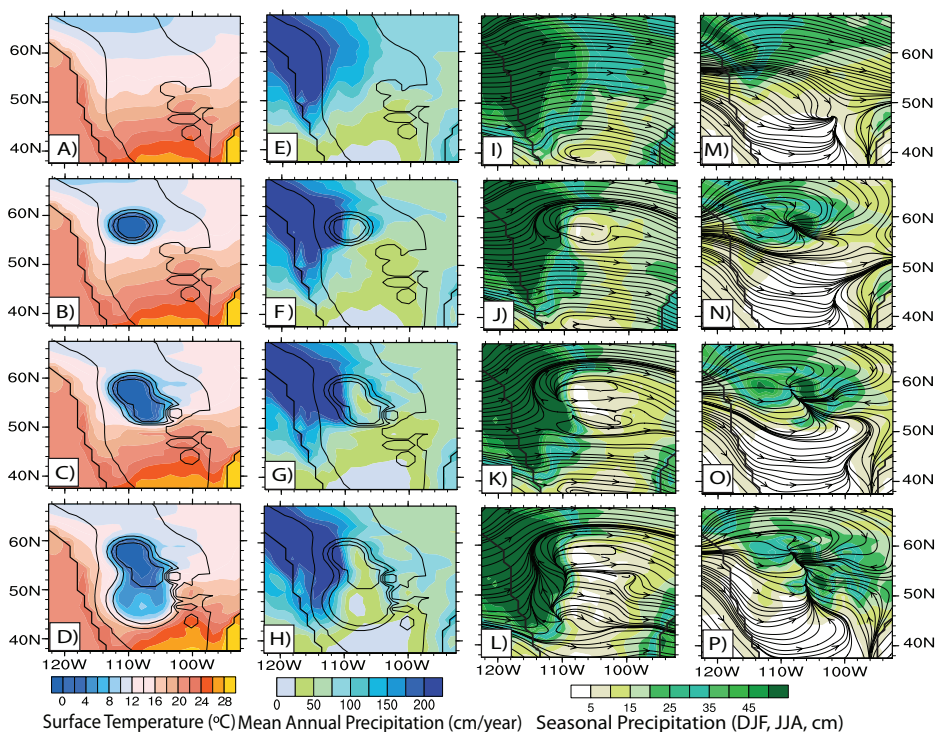
Fig. 4. Simulated western North American climate for CNTL (first row), NHL (second row), CHL (third row), and SHL (fourth row) scenarios. (A-D) Mean annual surface temperature (°C); (E-H) mean annual precipitation rate (cm yr$^{-1}$); (i-l) winter (December, January and February, DJF) precipitation (cm) and 850 hPa circulation (I-L); and (M-P) summer (June, July and August, JJA) precipitation (cm) and 850 hPa circulation. Thick black contours indicate the continental shoreline. Thin black lines in a–h represent elevation from 900 to 3600 m with 900 m interval. Notice the development of the paleo-North American Monsoon in O–P as indicated by summertime airflow from the paleo-Gulf of Mexico.

elevation basins and valleys (fig. 5). Simulated surface temperatures are systematically warmer than paleofloral temperatures estimated using the Climate Leaf-Analysis Multivariate Program (CLAMP), but are generally within 3 °C. Some of the disagreement may be due to an underestimate of surface temperatures by CLAMP, which tends to produce temperature estimates that are ~2 °C lower than those from the Leaf Margin Analysis method (Wing and Greenwood, 1993). A systematic underestimate of leaf size by CLAMP may cause the paleotemperatures to be too cool by an additional 1 °C (Peppe and others, 2010).

The dating of most Middle and Late Eocene floras is not precise enough to unambiguously assign them to a specific uplift scenario. Nevertheless, an apparent cooling trend inferred from the Late Eocene floras may be consistent with regional surface uplift. Paleofloras from Florissant (central Colorado), Salmon (central Idaho) and Copper Basin formations (upper northeast of Nevada) have temperature estimates ranging from 7.6 to 12.4 °C (Wolfe, 1994) much cooler than the nearby sites of early Eocene age such as Kisinger Lake (15.7 − 16.8 °C) and Green River Formation (14.3 − 16.7 °C) (fig. 5). Although some of this cooling is undoubtedly associated with Late Eocene global climate cooling (Wolfe, 1994), it may also reflect the development of high elevations through topographic migration (figs. 4B-4D).
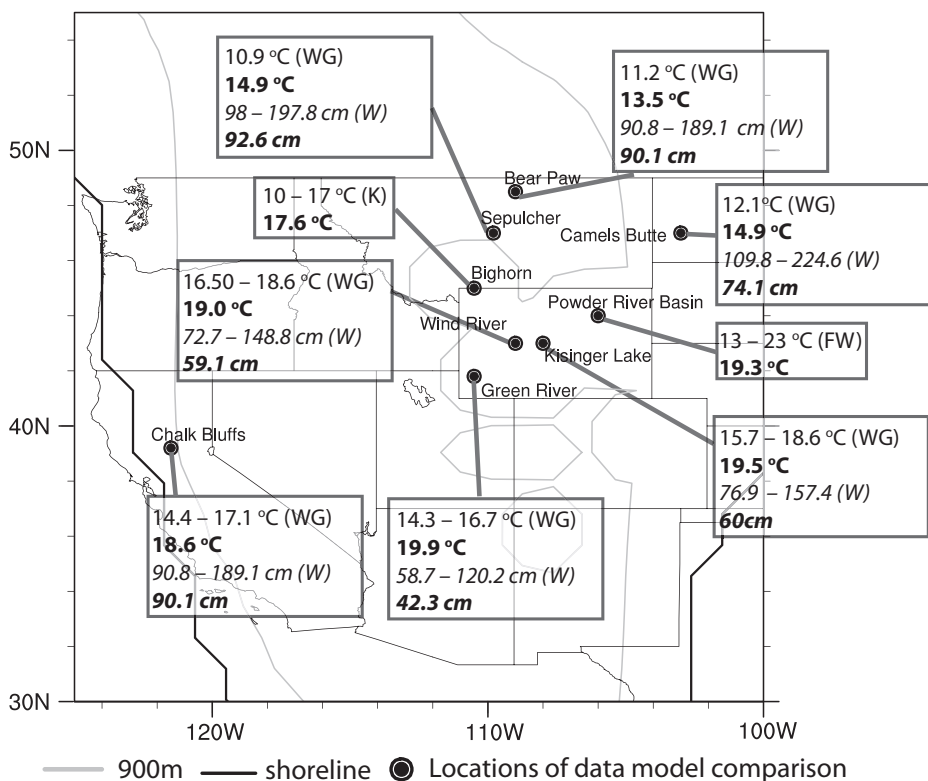
Fig. 5. Comparison between simulated (bold font) and proxy (regular font) surface temperature and precipitation (in italics) reconstructed from paleoflora of western North America (black dots). WG: Wing and Greenwood, (1993); W: Wilf and others (1998); K: Koch and others (1995); FW: Fricke and Wing (2004). The ranges of proxy temperatures are reported from the individual studies. The ranges of proxy precipitation are reported as the averages added with the uncertainties of estimations of precipitation.

### Simulated Early Eocene Precipitation of Western North America

Mean annual precipitation (MAP) in the CNTL experiment exhibits a northwest-southeast trend with maximum of 393.4 cm yr$^{-1}$ in the Pacific Northwest region and minimum of 10.9 cm yr$^{-1}$ over southwestern North America (fig. 4E). The inclusion of the highlands leads to formation of orographic precipitation on both sides of the mountains and precipitation minima on the eastern side of the highland interior (figs. 4F-4H).

Windward precipitation occurs mainly during winter (December-February, figs. 4I-4L) and results from forced ascent of westerly air masses over the mountain barrier. Diabatic cooling occurs on and around the top of the high Cordillera and facilitates condensation and snow formation. The southward propagation of the highlands significantly increases the amount of winter windward precipitation (figs. 4I-4L) and the portion of precipitation falling as snow (from 10% in CNTL to 28%, 38%, and 54% in NHL, CHL, and SHL experiments averaged over 40-60° N, 120°-110° W). In summer, warming of the mountain flank and weakening of the Westerlies reduces relative humidity and moisture transport, decreasing precipitation along the higher latitude coast (50°-60° N, 120°-115° W, figs. 4M-4P). On the western side of the highland peaks, localized increases of summer precipitation occur in the NHL and CHL experiments, likely due to cooling and condensation induced by high elevation.

Leeward precipitation falls mostly in summer (June-August, figs. 4M-4P) with a substantial portion occurring as convective precipitation. The moisture source of leeward precipitation is generally thought to come from below cloud-base evaporation and/or mixing with moisture-bearing air masses other than those traveling directly across the mountains (Gat and Rietti-Shatti, 1999). Consistent with this interpretation, simulated middle-to-low atmosphere water vapor has high deuterium excess (14-16‰) over this region, indicating the likely contribution of moisture from both surface and below cloud-base evaporation. The migrating topography induces north-to-south propagation of summer wetness in the lee of the highlands. As a result of surface uplift and topographic blocking, westerly flow is split into northern and southern branches (note streamlines in figs. 4M-4P). These two branches converge in the lee of the highland, promoting frontal development between cold, dry air from the north and warm, moist air from the south and high precipitation rates in NHL and CHL (figs. 4M-4P). The transport of Pacific moisture through the southern branch of the Westerlies is weaker in SHL due to blocking (compare streamline densities at 56° N, 120° W to 52° N, 110° W in figs. 4N-4P). The southward propagation of high topography promotes southeasterly moisture transport from the Gulf of Mexico. This summer southeasterly flow, which emerges in the CHL case (fig. 4O) but is most strongly expressed in SHL, represents a seasonal wind reversal and, as such, signifies the development of the paleo-North American Monsoon system.

The annual mean precipitation in the CNTL simulation is within 30 percent of estimates based on early Eocene paleofloral reconstructions by Wilf and others (1998). We speculate that the mismatch results from uncertainties related to taphonomical biases, leaf area analysis of fossil leaves and the possible underrepresentation in our simulation of local water bodies, such as small lakes and rivers. The pattern of precipitation is comparable to that simulated for the Paleogene using a higher resolution limited-domain model (Sewall and Sloan, 2006).

### $\delta^{18}O_p$ Response to Surface Uplift

In the absence of significant topography, simulated western North American $\delta^{18}O_p$ is mainly a function of latitude and continentality (fig. 6A). In the interior of the continent (between 115° and 90° W), $\delta^{18}O_p$ is zonal and decreases with latitude. Along the coastlines, $\delta^{18}O_p$ is high due to the proximity of $^{18}O$- and D-enriched moisture sources.

In ECHAM5-wiso, $\delta^{18}O_p$ strongly decreases with surface uplift of the Western Cordillera (figs. 6B-6D). Along the crest of the highlands, $\delta^{18}O_p$ drops by ~10 permil to values less than −18 permil forming sharp isotopic gradients on the flanks. With southward propagation of the highlands, precipitation in foreland areas east of 100° W become enriched in $^{18}O$ due to the contribution of moisture from the paleo-Gulf of Mexico (fig. 6D).

Proxy estimates of $\delta^{18}O_p$ derived from authigenic minerals require knowledge of the isotope exchange temperature, the temperature of the water from which the mineral precipitated. In the absence of this information, Mix and others (2011) and Chamberlain and others (2012) use temperatures from paleofloral assemblages as the isotope exchange temperature. To directly compare simulated and proxy $\delta^{18}O_p$ and eliminate differences due to surface temperature assumptions, we recalculate mineral-derived $\delta^{18}O_p$ using simulated surface temperatures (Appendix D, table D1). Because isotopic fractionation has only a small temperature dependence (~0.2‰ °C$^{-1}$ at 25 °C for carbonate), most proxy $\delta^{18}O_p$ estimates change by ≤2 permil. The exceptions are two samples from the Galisteo Basin of New Mexico (Davis and others, 2009), with ages of 39 to 49 (3.6‰) and 28 to 39 Ma (5.2‰), and two samples (2.1‰), with ages of 39 to 49 Ma, from eastern Wyoming (Sjostrom and others, 2006). These samples, all from low altitude basins, were originally assigned isotope exchange
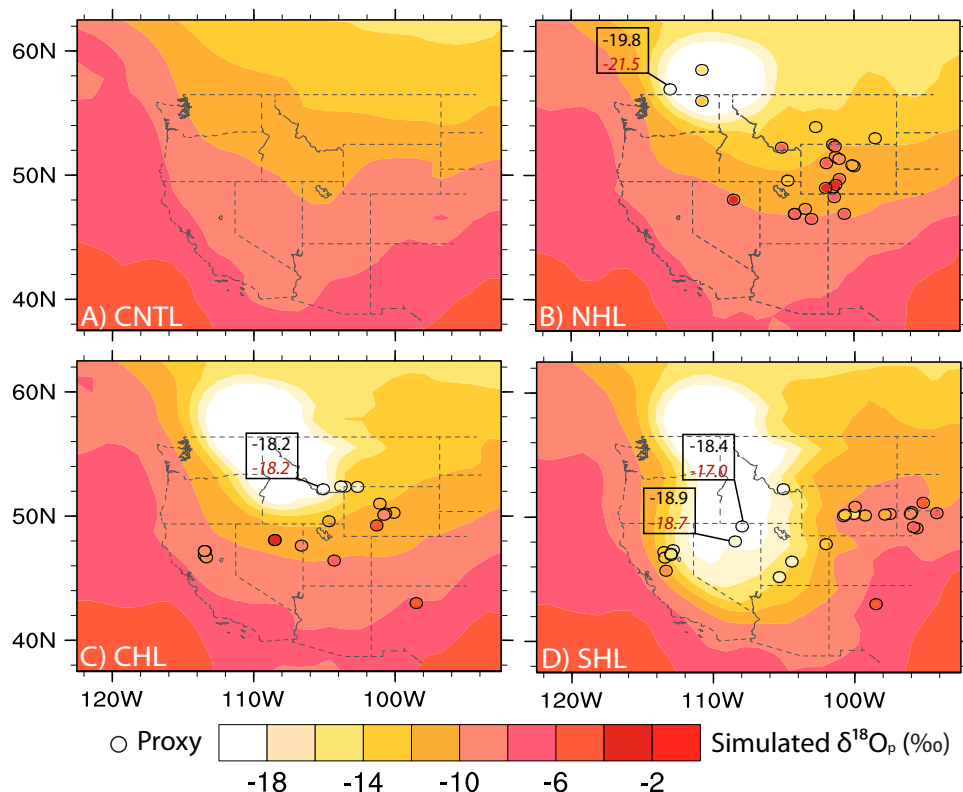
Fig. 6. Comparison of proxy and simulated $\delta^{18}O_P$. Simulated values of $\delta^{18}O_P$ are shown for the (A) CNTL, (B) NHL, (C) CHL, and (D) SHL experiments. Following Mix and others (2011) and Chamberlain and others (2012), the NHL, CHL, and SHL scenarios represent topographic conditions in western North America ranges across approximately pre-49 Ma of Eocene, 48–39 Ma, and 38–28 Ma. Proxy $\delta^{18}O_P$ from authigenic minerals corresponding in age to these time intervals are overlain as filled circles. Simulated (black font) and mineral (red font) $\delta^{18}O_P$ are shown for the Princeton Basin (B), Sage Creek Basin (C), and Copper (north) and Elko (south) Basins (D). U.S. state borders are shown to simplify the referencing of sample locations. The borders have been modified to account for Neogene Basin and Range extension by narrowing Nevada by ~2° longitude as in figure 1.

temperatures of 7.5 °C, 0 °C and 10.9 °C, much lower values than the simulated temperatures of 24.5 °C and 24.1 °C for the Galisteo Basin and 20.8 °C for eastern Wyoming. For comparison, modern mean-annual temperatures in the Galisteo Basin and eastern (Casper) Wyoming are ~11 and ~9 °C. Early Eocene paleotemperatures for the Wind River, Kisinger Lake and Powder River basin, located in central and eastern Wyoming, are 16.5 to 23 °C (fig. 5).

In figures 6B–6D, we compare simulated $\delta^{18}O_P$ from our three topography scenarios with temperature-adjusted proxy $\delta^{18}O_P$. Co-located simulated and proxy $\delta^{18}O_P$ agree within 2 permil at 60 percent of sites (figs. 6B-6D). Differences within this group have an average of 0 permil with a $1\sigma$ value of 1.1 permil, indicating no systematic offset. More importantly, there is good correspondence in all three scenarios between very low values ($< -16$ ‰) of simulated and proxy $\delta^{18}O_P$. Mix and others (2011) use mineral $\delta^{18}O_P$ from four sites (Princeton Basin, Sage Creek Basin, Copper Basin, and Elko Basin) to estimate maximum highland elevations (fig. 6, values in black). Our simulated $\delta^{18}O_P$ at these sites is the same or slightly lower (with magnitude $< 2$‰) than the mineral $\delta^{18}O_P$ (fig. 6, values in red). The good match

indicates that surface uplift is a reasonable hypothesis for explaining temporal trends in the mineral proxies.

$\delta^{18}O_p$ difference for the remaining 40 percent of sites averages $-2$ permil with a $1\sigma$ value of 4.5 permil. Many of the points of disagreement occur in the NHL case and are located in the Laramide foreland basins east of $102°$ W and in the Elko Basin in northeast Nevada, regions of low elevation. The mismatch at these lowlands may be due to surface hydrologic processes that are not included in ECHAM5-wiso. Many of the enriched $\delta^{18}O$ values from the Laramide foreland basins and northeastern Nevada and central Utah derive from lacustrine carbonates and limestones. The hydrological balance of inland lakes is a function of riverine, groundwater, and precipitation inputs, and evaporative losses. Unless precipitation dominates the system, lake water $\delta^{18}O$ may not reflect $\delta^{18}O_p$. In fact, Horton and others (2004), Bowen and others, (2008) and Davis and others (2009) conclude that Elko Basin, Flagstaff Basin and other Laramide foreland basins have all been affected by significant evaporation.

Notable mismatches also occur at four high-elevation sites, including two in the core of the NHL (fig. 6B) and two on the eastern flank of the SHL (fig. 6D). The mineral samples from the NHL have $\delta^{18}O_p$ of $-13.8$ and $-15.8$ permil, values that correspond to simulated $\delta^{18}O_p$ at elevations of $\sim$2000 m (fig. 7A). The mineral $\delta^{18}O_p$ at these locations are converted from the $\delta D$ of mylonitic quartzite in equilibrium with the meteoric water at the Columbia River detachment bounding Kettle (northeast Washington) and Shuswap metamorphic core complex (southeast British Columbia). The reconstructed $\delta^{18}O_p$ of these locations is likely more enriched than the actual meteoric water due to water-rock interaction (Mulch and others, 2007). However, the isotopic enrichment could also indicate that the highland elevations are overestimated, or that these proxies record elevation of the detachment, which may be lower than the mean elevation. Mineral $\delta^{18}O_p$ on top of the eastern flank of the SHL (the Claron Basin and the Flagstaff Basin) is lower by 2 to 3 permil than the simulated $\delta^{18}O_p$.

*Analysis of Isotopic Fractionation Due to Lifting*

Paleoaltimetry studies have traditionally assumed that the isotopic composition of an ascending air mass fractionates through rainout as a result of adiabatic cooling and condensation (for example, Blisniuk and Stern, 2005). This assumption is the premise for both the application of empirical $\delta^{18}O_p$-lapse rates and RDMs to paleoaltimetry. To evaluate this assumption, we compare GCM and RDM simulations of $\delta^{18}O_p$ across the highlands (figs. 7A-7F). RDM predictions are based upon GCM-initial $\delta^{18}O_v$, and with moisture sources located both west and east of the flanks of individual highland [see *Rayleigh Distillation Model of Adiabatic Condensation* (*RDM*) section for details]. Justification for an eastern moisture source is shown in figures 4N–4P, which illustrates that summer flow onto the eastern flanks of the highlands is predominantly easterly across the continental interior. Our one-dimensional RDM simulations of $\delta^{18}O_p$ vary solely as a function of altitude; the horizontal trajectory of the parcel is not considered. To more straightforwardly compare the GCM and RDM, we remove $\delta^{18}O_p$ spatial variability in our GCM simulations by averaging annual $\delta^{18}O_p$ over a range of latitudes centered on the NHL, CHL and SHL.

The relationship of mean-annual $\delta^{18}O_p$ with altitude differs substantially between the GCM and RDM with *GCM-moisture* source (dots and crosses in figs. 7A-7F). GCM-simulated $\delta^{18}O_p$ decreases nonlinearly with elevation on both flanks. The isotopic lapse rate is greatest at elevations lower than $\sim$2000 m, particularly on western slopes, and decreases to nearly 0 at higher elevations in the NHL and CHL cases (filled circles in figs. 7A and 7B). In comparison, RDM-simulated $\delta^{18}O_p$ decreases almost linearly with elevation with the highest lapse rate on the eastern flanks (crosses in figs. 7D-7F). At peak elevations on the western flank, RDM and GCM $\delta^{18}O_p$ are relatively
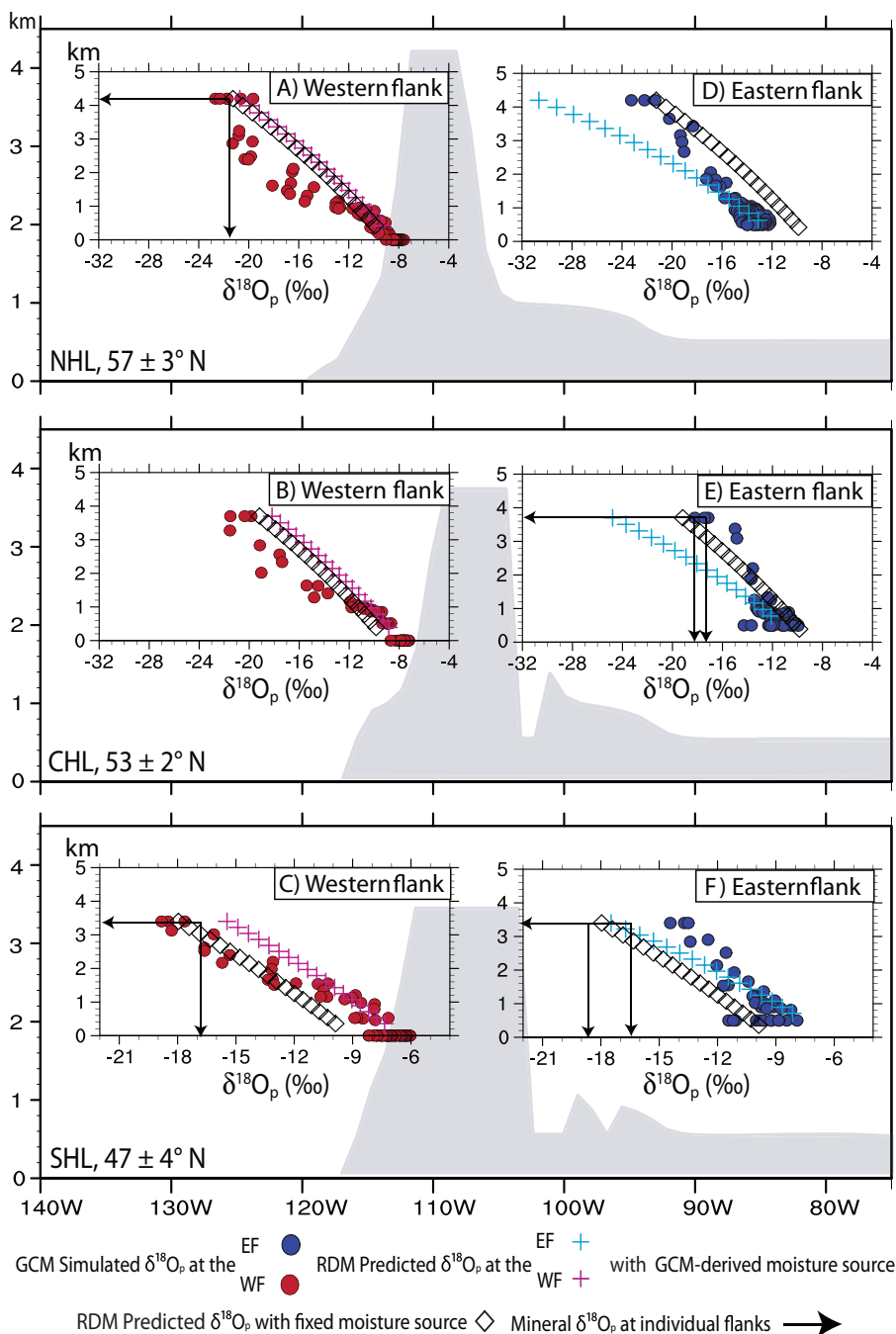
Fig. 7. Comparison of GCM and RDM $\delta^{18}O_p$ along the western and eastern flanks of the northern [NHL, (A) and (D)], central [CHL, (B) and (E)], and southern [SHL, (C) and (F)] highlands. ECHAM5-wiso $\delta^{18}O_p$ is shown as filled circles; $\delta^{18}O_p$ simulated by the RDM with fixed initial $\delta^{18}O_v$ and moisture from the west as open diamonds (values at the eastern flank mirrors those at the western flank since they share the same moisture sources); and $\delta^{18}O_p$ simulated by the RDM with GCM-derived initial $\delta^{18}O_v$ and moisture from both western and eastern flank as crosses. Symbols are shaded red and blue to indicate their location on either western (WF) or eastern flanks (EF). The extents of western and eastern slopes are shown in figures 3A–C Arrows point to mineral $\delta^{18}O_p$ values at 4200 m of NHL, 3700 m of CHL and 3400 m of SHL. Notice that the elevations of the mineral-derived $\delta^{18}O_p$ are uncertain. The best estimate of the elevation is where the mineral-derived $\delta^{18}O_p$ values correspond to simulated $\delta^{18}O_p$.

similar in NHL and CHL, differing by about $+1$ permil (NHL) and $-1$ permil (CHL) (compare crosses and filled circles in figs. 7A and 7B). RDM and GCM $\delta^{18}O_p$ differences are much larger, about $-3$ permil, in SHL (compare crosses and filled circles in fig. 7C). However, due to differences in isotopic lapse rates, the $\delta^{18}O_p$ difference is much larger (by as much as 5‰) at intermediate elevations between ~1000 and 3000 m (figs. 7A-7B). $\delta^{18}O_P$ differences are more pronounced on the eastern slopes, where the RDM isotopic lapse rates are very high, leading to very low $\delta^{18}O_p$ (compare light gray markers in figs. 7A-7C). At peak elevations on the eastern flank, the RDM and GCM $\delta^{18}O_p$ differ by approximately 9 (NHL), 6 (CHL) and 4 permil (SHL).

The influence of assuming a constant moisture source is demonstrated by the difference between experiments with *fixed-* and *GCM-moisture* sources (figs. 7A-7C). Along the western flanks, $\delta^{18}O_p$ is offset by the difference in the composition of the initial condensate, which is minimal for NHL and CHL but approximately $-3$ permil for SHL. Along the eastern flank, $\delta^{18}O_p$ differences are greater, up to 6 to 8 permil at high elevations of the NHL and CHL, and result from differences in temperature and humidity of the moisture source and the $\delta^{18}O_p$ of initial condensate. Adiabatic cooling and rainout are more dramatic for cooler and drier moisture sources at the eastern flank, which leads to larger adiabatic lapse rate of the $\delta^{18}O_p$.

Our comparison of $\delta^{18}O_p$ estimated by ECHAM5-wiso and an RDM emphasizes the importance of the interaction of different airflow regimes and precipitation physics other than rainout on the isotopic fractionation of vapor and precipitation in the GCM. In the following sections, we investigate these processes.

### Influence of Precipitation Type on $\delta^{18}O_p$

ECHAM5-wiso simulates multiple precipitation phases (snow and rain) and types (convective, large-scale). At low elevations ($\leq$1500 m) on the western flanks of the NHL, CHL, and SHL, the bulk of the precipitation is in the form of large-scale rainfall. In this region, GCM-simulated $\delta^{18}O_p$ is similar to the RDM prediction. The difference between GCM- and RDM-simulated $\delta^{18}O_p$ increases as contributions from snowfall and convective precipitation increase at higher elevations of the western and eastern flank. Snow and convective precipitation contribute differently to the $\delta^{18}O_p$ of total precipitation (figs. 8D-8F). Snow is more depleted in $^{18}O$ than other precipitation types, because ice crystal condensation is subject to kinetic fractionation due to the lower diffusivity of the heavy isotope in air (Jouzel and Merlivat, 1984); and, isotopic exchange between snowfall and the environment through evaporation, mixing, and re-condensation below the cloud base is greatly reduced (Jouzel and Merlivat, 1984; Gat, 2010). Convective precipitation is enriched in $^{18}O$ relative to the total precipitation across the highlands, but is more depleted at the coast (figs. 8D-8F). Leeside convective precipitation is enriched in $^{18}O$ likely due to intense evaporation of rain droplets and/or mixing with isotopically enriched moisture, a mechanism proposed to explain the enrichment of modern leeside precipitation (Gat and Rietti-Shati, 1999). This process is the counterpart to the "amount effect" in tropic regions where limited sub-cloud evaporation and the input of $^{18}O$ depleted moisture occurs, causing isotopic compositions to be relatively low (Risi and Vimeux, 2008).

Snowfall occurs on the western flanks at elevations higher than 1000 m and is the main form of precipitation on the western highlands (figs. 8A-8C, medium gray lines). Convective precipitation is common over lowlands and on the flanks but is absent at the highland top. On average, it makes up one-third to one-half of total annual precipitation on the eastern flanks (figs. 8A-8C, light gray lines), and increases to one-half to three-fourth of total precipitation during summer (not shown). Moist convection is almost absent in winter, indicating a strong seasonality of the $^{18}O$ enrichment effect due to moist convection. The relative contribution of snow and
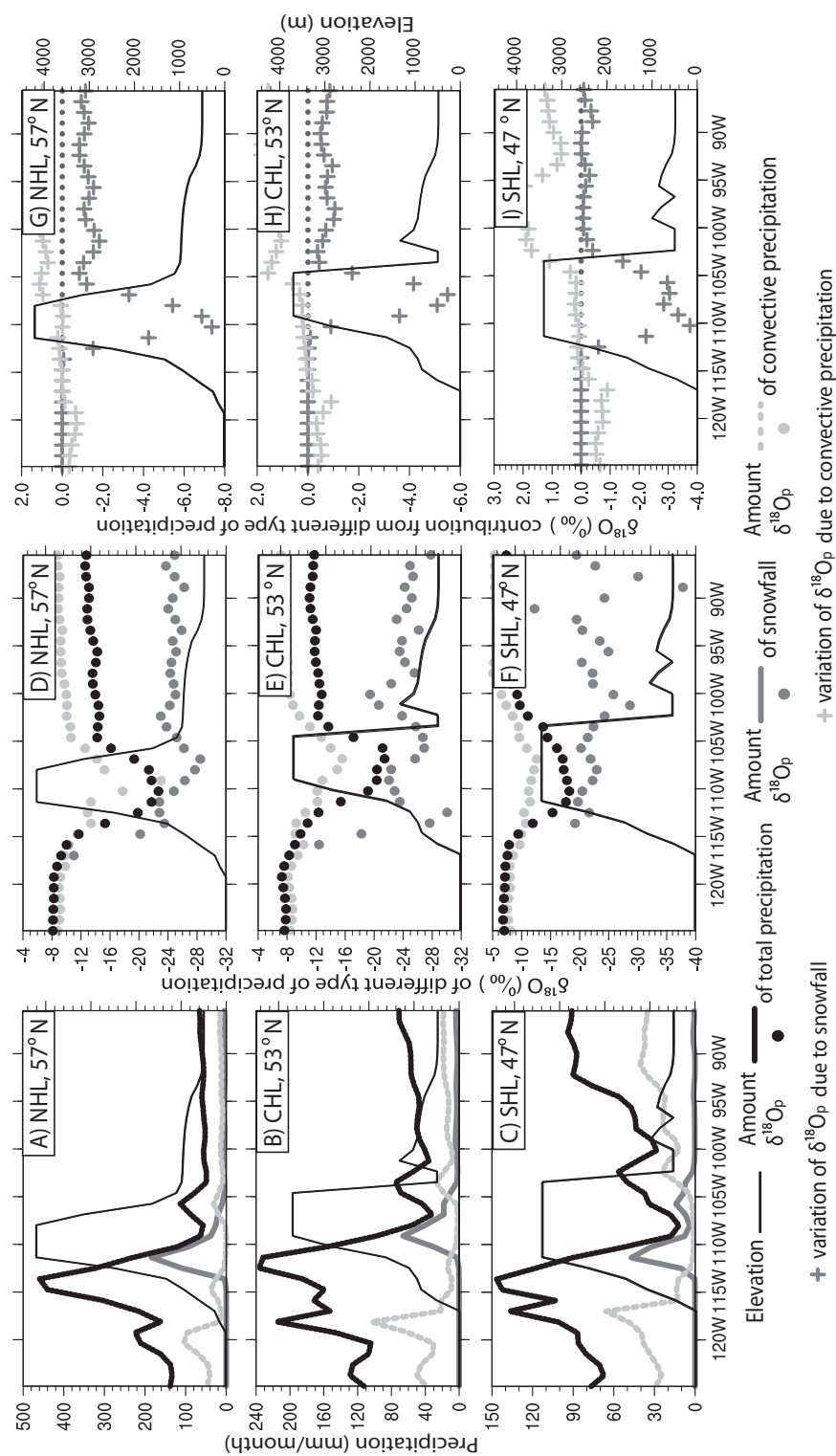
Fig. 8. Simulated west-east distribution of the amount (A-C, left column) and δ¹⁸O (D-F, middle column) of total precipitation (dark gray), snowfall (medium gray) and convective precipitation (light gray). The δ¹⁸Oₚ variations (G-I, right column) due to inclusion of snowfall (medium gray) and convective precipitation (light gray) at 57 locations on either western (WF) or eastern flanks (EF). The extent of western and eastern slope-scale (A-I, black). The snowfall is from both large-scale and convective precipitation, but it is clearly from large-scale at the western flank and likely from both at the eastern flank.

convective precipitation to $\delta^{18}O_p$ is estimated as the difference of $\delta^{18}O_p$ in the absence of snow or convective precipitation:

$$\Delta[\delta^{18}O_p]_i \approx r_i \times ([\delta^{18}O_p]_i - [\delta^{18}O_p]_o)$$

where $[\delta^{18}O_p]_i$ is the $\delta^{18}O_p$ value of snow or convective precipitation; $[\delta^{18}O_p]_o$ is the $\delta^{18}O_p$ of the remaining precipitation; and $r_i$ is the ratio of snow or convective precipitation to total precipitation.

High-elevation snowfall reduces the total $\delta^{18}O_p$ across the highlands and by up to 4 to 8 permil at the peaks (figs. 8G-8I). Convective precipitation increases $\delta^{18}O_p$ on the leeside of the highlands by up to ~2 permil (figs. 8G-8I, light gray cross). Snowfall and convective precipitation influence $\delta^{18}O_p$ in opposing ways on the eastern slopes. The relative amounts of convective precipitation and snowfall and their contribution to total precipitation $\delta^{18}O_p$ are not necessarily independent; snow can form from condensation related to large-scale and/or convective processes. Condensation of convective snow enriches the remaining vapor from which subsequent convective precipitation might condense. This possibility is supported by the anti-correlation between snow and convective precipitation $\delta^{18}O_p$ on the eastern lowlands of the NHL and CHL cases (figs. 8G-8H).

Independent geological lines of evidence support the simulation of both snowfall on the highlands and seasonally arid conditions at the leeside of the highlands. Eocene lacustrine bivalves collected from the Green River Basin (Norris and others, 1996) and Power River Basin (Dettman and Lohmann, 2000; although disputed by Morrill and Koch, 2002) and fossil tooth enamel (Fricke, 2003; Fricke and Wing, 2004) and paleosol carbonates collected from the Big Horn Basin (Koch and others, 1995) record seasonal low $\delta^{18}O$ that are purported to represent seasonal snow melt and drainage from adjacent highlands. Pedogenic features (Bown and Kraus, 1981), evaporite deposits (Smoot, 1983), and dry-tolerant paleoflora (Wolfe, 1994; Wing and Greenwood, 1993; Wilf and others, 1998) have all been interpreted to indicate seasonal drought or evaporative conditions on the leeside of the highlands. In addition, paleoprecipitation reconstructions from paleoflora within three foreland basins around Green River, Kisingers Lakes and Wind River support high precipitation seasonality with one-half of the precipitation falling in three growing months and ≤10 percent in three dry months (Wing and Greenwood, 1993), and lend support to our simulations of intense summer precipitation and winter dryness (figs. 4M-4O).

### *Influence of Vapor Mixing on $\delta^{18}O_p$*

Isotopic effect of advective vapor mixing is most pronounced on the western slopes of the highlands. In this region, upslope flow contributes substantially to vapor $^{18}O$ enrichment. In the middle troposphere (500-600 hPa), $\delta^{18}O_c$ advection is alternately positive, negative and positive at the western flank, highland top and eastern flank of NHL and CHL. This pattern reflects vertical advection associated with a standing gravity wave (figs. 9A and 9B, vectors and gray contour) that develops as the Westerlies encounter high topography. This standing gravity wave is not as well pronounced in SHL; as a result, the $\delta^{18}O_c$ advection across the SHL is determined by both the vertical and horizontal advection of the air mass. Positive $\delta^{18}O_c$ advection is brought by ascending air masses from lower altitudes at the western flanks and by southeasterly flow from lower latitudes at the eastern flank (fig. 4P), which lead to locally high $\delta^{18}O_v$ regions.

$^{18}O$-enrichment due to mixing can explain the flattening of the GCM-simulated $\delta^{18}O_p$-elevation relationship of NHL (fig. 7A) and CHL (fig. 7B) at elevations >2000 m. The influence of mixing on the western slope of the SHL is less apparent (fig. 7C); precipitation likely forms over a range of altitudes that are both isotopically depleted
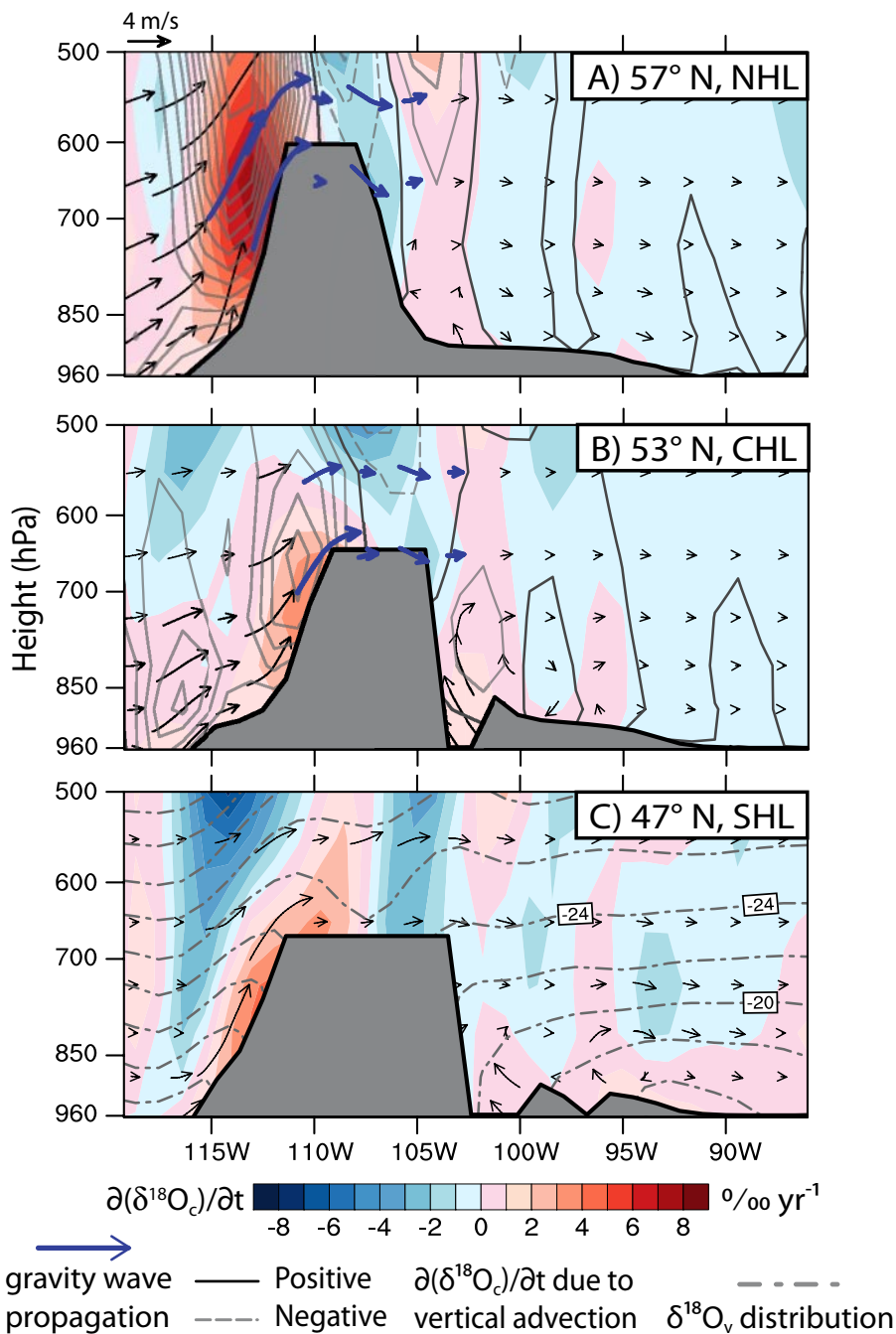
Fig. 9. Zonal distribution of variations of $\delta^{18}O$ of condensate $\left(\dfrac{\partial\delta^{18}O_c}{\partial t}\right)$ due to the total (shaded) advection of moisture estimated at (A) 57°N of NHL case, (B) 53°N of CHL case and (C) 47°N of SHL case. Solid and dashed gray contours in (A) and (B) show positive and negative $\left(\dfrac{\partial\delta^{18}O_c}{\partial t}\right)$ at interval of 0.5‰ yr$^{-1}$ due to vertical advection of moisture. Dotted gray contours in (C) shows the zonal distribution of $\delta^{18}O_v$. The zonal circulations and mountain gravity wave trajectories are shown in black and thick blue arrows.

and enriched through mixing (fig. 9C). The $\delta^{18}O_c$ variations due to mixing at the eastern flank are generally small with magnitudes of $\leq 2$ permil and vary in sign from the surface to the middle troposphere.

### *Influence of Moisture Recycling Through Surface Exchange on $\delta^{18}O_p$*

In arid, continental regions, observed $\delta^{18}O_p$ lapse rates are often smaller than expected based on open system Rayleigh distillation models (for example, Blisniuk and Stern, 2005; Rowley and Garzione, 2007; Lechler and Niemi, 2011). This phenomenon, referred to as a "pseudo-altitude effect," is thought to result from an increase in evaporative enrichment of a rain droplet as the falling distance increases from the top to the bottom of the mountain (Moser and Stichler, 1971). Another potentially important factor is the $^{18}O$-enrichment of vapor through recycling at the land surface. During the recycling process, surface evaporation enriches and returns much of the precipitation to the boundary layer. In our simulations, vapor recycling is vigorous on the leeside eastern flanks, where evaporation rates are typically 70 to 76 percent of precipitation rates. Moisture recycling is less important at the western flank, given that the air mass are more humid and the amount of evaporation is less than 30 percent of precipitation.

We have modified the RDM to account for vapor recycling using the recycling potential estimated using GCM-simulated rates (see *Rayleigh Distillation Model of Adiabatic Condensation (RDM)* above). Recycling potentials for the NHL, CHL and SHL experiments are 0.68, 0.73, and 0.76. Accounting for vapor recycling in the RDM increases $\delta^{18}O_p$ on the eastern slopes by ~3 to 5 permil, reducing the isotopic lapse rate and the discrepancy between GCM and RDM $\delta^{18}O_p$ in this region (figs. 10A-10C).

### *Influence of Moisture Sources on $\delta^{18}O_p$*

Moisture sources are expected to change as circulation patterns evolve in response to surface uplift (figs. 4I-4P). Back trajectory analyses of air parcels originating on the mountain flanks are performed to identify moisture sources in each topographic scenario (figs. 11 and 12). In the CNTL case, low-level airflow over western North America is predominantly westerly and originates from the northern side of the Pacific subtropical high (figs. 11A-11C, colored thin lines). Over the continent, flow splits into northern and southern branches at ~50° N (hereafter referred to as "split flow"; gray lines with black arrows in figs. 11A-11C) in response to the development of high-pressure ridges over the western side of the topography.

Topographic uplift and southward propagation enhances the separation of northern and southern branches by strengthening the high-pressure ridge to the west and partially blocking the airflow. The split flow affects the moisture path, which then influences the isotopic composition of vapor. At the western flank, all three highlands (NHL, CHL and SHL) receive air parcels that originate over the northeast Pacific. Air parcels are transported by westerly flow to the NHL and CHL (figs. 11D-11E). Air parcels at SHL, however, are transported across warmer low-latitude seawater by northwesterly winds following the southern branch of the split flow along the coast (fig. 11F). As a result, the moisture source of SHL is more humid and more enriched in $^{18}O$ than the moisture source of the NHL and CHL (figs. 3A-3C). Galewsky (2009) reports based on a series of simulations with idealized topography that blocking and lateral deflection by high topography reduces orographic precipitation and increases $\delta^{18}O_p$. In our simulations, blocking is not complete; flow ascends the western flanks, promoting orographic precipitation (figs. 4E-4L and fig. 9).

Surface uplift changes moisture transport to the lee of the mountains as well. In the absence of high topography, air parcels are transported to the east flank by a mixture of both northern and southern branches of the split flow (colored thin lines in figs. 12A-12C). With uplift, leeward moisture in NHL and CHL mostly derives from the
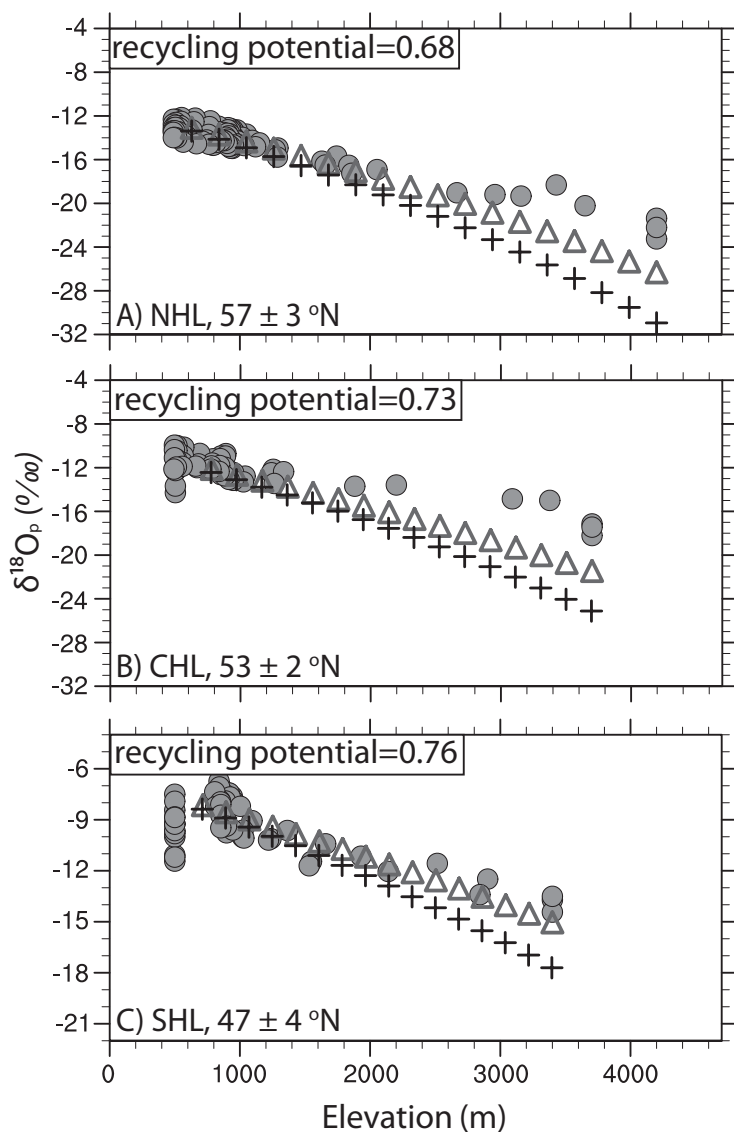
Fig. 10. Comparison of $\delta^{18}O_p$ simulated by GCM, RDM and RDM with vapor recycling on the eastern flanks (EF) of (A) northern (NHL), central (CHL), and southern (SHL) highlands. In A–C, ECHAM5-wiso $\delta^{18}O_p$ is shown as filled circles; RDM $\delta^{18}O_p$ with moisture recycling as open triangles; RDM $\delta^{18}O_p$ without moisture recycling as crosses. The incorporation of moisture recycling on the lee of the highlands increases RDM $\delta^{18}O_p$ by several permil, bringing it in closer agreement with GCM $\delta^{18}O_p$.

southern branch of the split flow (figs. 12D-12E). In the SHL scenario, the paleo-Gulf of Mexico is the dominant source of leeside moisture (fig. 12F). Surface uplift also introduces strong precipitation and circulation seasonality on the leeside of the mountains (figs. 4I-4P).
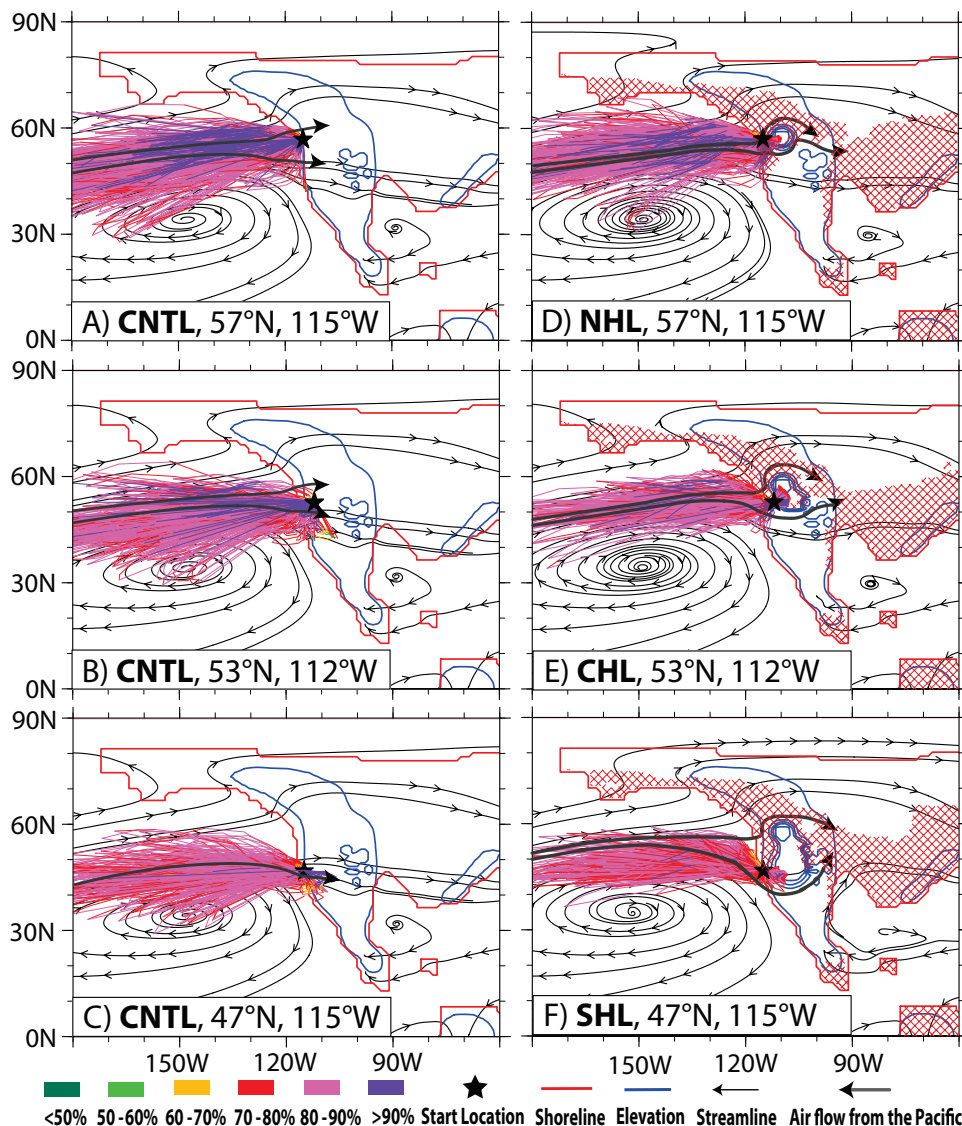
Fig. 11. Back trajectory analysis of highland air parcels from the western flank of highlands. The 7-day back trajectory location and relative humidity of air parcels are shown (as colored thin lines) for CNTL (A-C) and NHL (D), CHL (E), and SHL (F). Each line segment is colored with the average relative humidity of a single trajectory within one time interval. Also shown in each figure are the low-level circulation (streamlines, averaged from 850 to 1000 hPa); the start location of back trajectory (black star); topography (blue line); airflow path (grey line with black arrowhead); and the continental shoreline (red line). Areas with evaporation greater than 40 cm/month are indicated by red stipple. Notice that 1) topography enhances separation of the northern and southern airflow paths (compare NHL, CHL, and SHL scenarios with the CNTL case); and 2) air parcels on the SHL tend to originate from more southerly sources in comparison to those on NHL and CHL.

Eastern flank $\delta^{18}O_p$ is strongly influenced by the source of moisture. Moisture from the Pacific Ocean and land evaporation has relatively low $\delta^{18}O_v$ due to greater rainout over long travel distances and evaporation input from isotopically depleted
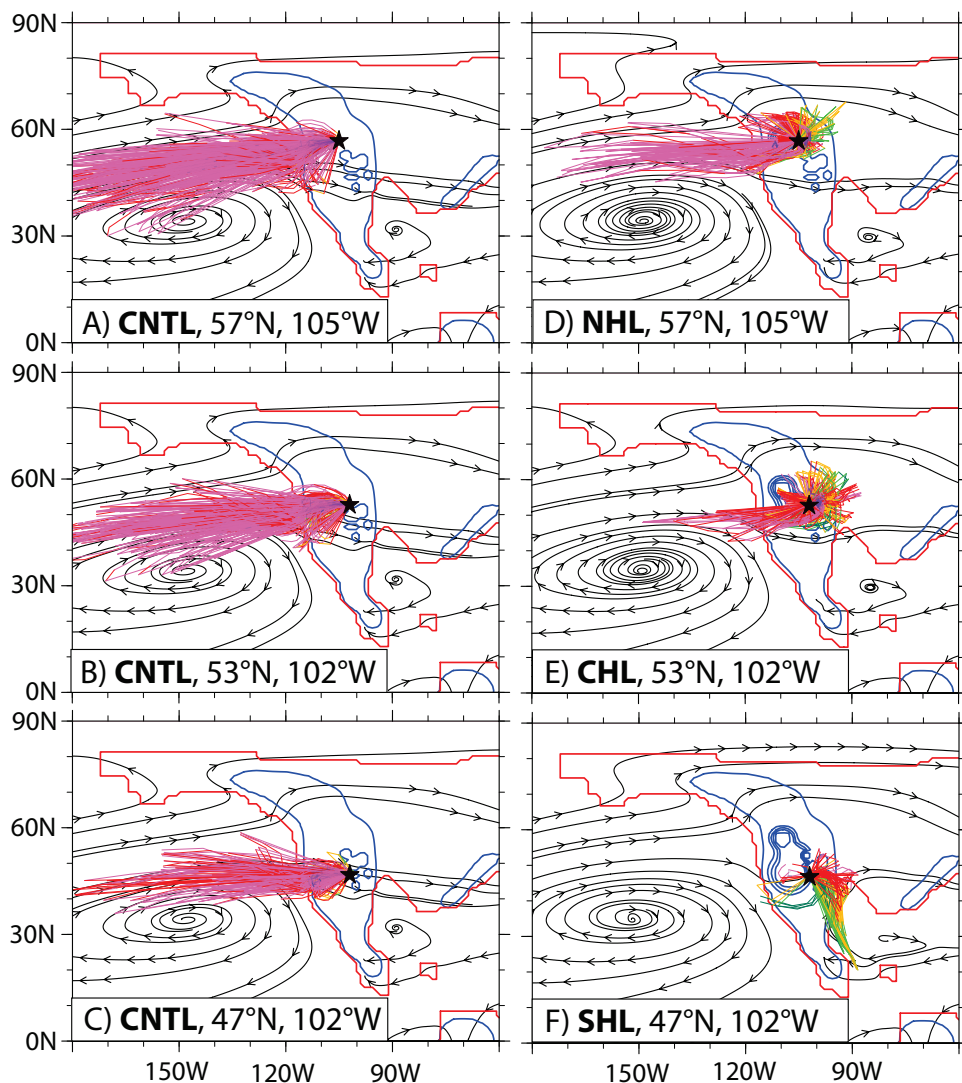
Fig. 12. Same as in figure 11, but for air parcels on the eastern flank of CNTL, NHL, CHL and SHL. Note that CNTL (pre-uplift) moisture sources (colored thin lines) originate mainly (not entirely) from the Pacific Ocean. In the NHL, CHL, and the SHL (post-uplift) scenarios, a greater portion of moisture sources to the leeside of the highlands originates from the continental interior and the paleo-Gulf of Mexico.

inland sources. In contrast, moisture from local lakes distributed within the Laramide basins and the paleo-Gulf of Mexico is enriched in $^{18}$O. As a result of these differences, eastern flank $\delta^{18}O_p$ of NHL and CHL, most of which is derived from a mixture of $^{18}$O-depleted land evaporation and east Pacific vapor with limited contribution from lakes (figs. 11D-11E, stippled pattern shows evaporation) and the paleo-Gulf of Mexico (figs. 12D-12E), is relatively low (figs. 3A-3C). On the eastern flank of SHL, the contribution from lake evaporation (fig. 11F, stippled pattern) and Gulf of Mexico moisture is greater (fig. 12F) and so is the $\delta^{18}O_p$.

*Contribution of physical processes to $\delta^{18}O_p$ in orographic regions. Values represent the approximate isotopic contribution (‰) of each process to the local $\delta^{18}O_p$ simulated by ECHAM5-wiso and are shown for the three topographic scenarios*

| | | Precipitation type[1] | Total mixing[2] | Varying moisture sources[3] | Vapor recycling[4] |
|---|---|---|---|---|---|
| NHL | Western flank | −4 to −8 | +5 to +8 | NA | NA |
| | Eastern flank | +2 | NA | −8 to −10 | +5 |
| CHL | Western flank | −3.5 to −6 | +4 | NA | NA |
| | Eastern flank | +2 | NA | −6 | +3 |
| SHL | Western flank | −2 to −3 | NA | +3 | NA |
| | Eastern flank | +2 | NA | NA | +3 |

[1] Calculated as the amount weighted difference of $\delta^{18}O_p$ of snowfall (western flank) or convective precipitation (eastern flank) minus the $\delta^{18}O_p$ in the absence of snowfall or convective precipitation at high elevations.

[2] Estimated as the advection potential of condensates along the flank.

[3] Measured as the difference of simulated $\delta^{18}O_p$ by Rayleigh distillation model between using *GCM-* and *fixed-moisture* source at high elevations.

[4]Estimated as the RDM simulation with the vapor recycling ratio minus without the vapor recycling ratio.

NA: Not appreciable; the contribution is small.

*Rayleigh Distillation as a Model for Isotopic Fractionation of Condensation*

The challenge of stable isotope paleoaltimetry is to accurately translate mineral proxy $\delta^{18}O_p$ to surface elevation. Modern empirical $\delta^{18}O_p$-elevation relationships are useful for calibration in the modern climate under the existing topographic regime. However, regional climate change related to both uplift (Poulsen and others, 2010) and global climate (Poulsen and Jeffery, 2011) alter these relationships, rendering the use of modern isotopic lapse rates for stable paleoaltimetry questionable at best. Incidentally, paleoaltimetry estimates using terrestrial paleotemperature proxies (for example, clumped isotopes) and modern temperature lapse rates are prone to many of the same uncertainties that plague isotope lapse rates. In our experiments, $\delta^{18}O_p$ lapse rates vary across the western North American Cordillera and are different from modern empirical lapse rates. $\delta^{18}O_p$ lapse rates on the western flanks of the NHL, CHL and SHL are not linear and differ substantially at low and high elevations. Although $\delta^{18}O_p$ varies with elevations in a more linear manner at the eastern flanks of the Cordillera, the $\delta^{18}O_p$ lapse rates vary with latitude and are influenced by regional climates that are different from modern. As such, applying a $\delta^{18}O_p$ lapse rate-elevation relationship to infer paleoaltimetry in the North American Cordillera is unjustified.

RDMs offer some advantages for paleoaltimetry over modern empirical $\delta^{18}O_p$-elevation relationships. Chief among these is that RDM estimates are not based on modern temperature and humidity conditions, and can account for isotopic fractionation during adiabatic lifting and vapor condensation under different climate conditions. However, as this study demonstrates, in some regions, RDMs provide poor or incomplete representations of $\delta^{18}O_P$ because they neglect many aspects of precipitation physics that can influence $\delta^{18}O_p$. GCMs have the benefit of including these processes. The isotopic variations due to the formation of different precipitation types, vapor mixing and recycling, varying moisture sources and their relative importance at the eastern and western flanks of the highlands are summarized in table 2.

On the western flank of the NHL and CHL, both snow and vapor mixing have a substantial influence on $\delta^{18}O_p$ (table 2). On the SHL, snowfall and moisture source are most important (table 2). These results highlight the fact that physical processes change with environment and with evolution of the mountain range. In the SHL experiment, for example, the presence of an extensive north-south plateau deflects westerly flow, altering circulation patterns and moisture sources. Coincidentally, in all three scenarios, the influence of physical processes on $\delta^{18}O_p$ are opposite in sign and compensate over the highlands (table 2). As a result, GCM and RDM $\delta^{18}O_p$ are similar within ~3 permil at maximum elevations on the western flank (figs. 7A-7C) and agree within ~2 permil with mineral proxy $\delta^{18}O_p$ (figs. 7A and 7C, indicated by intersection of vertical and horizontal arrows) with one exception (fig. 7C, note relatively high $\delta^{18}O_p$ indicated by cross marks). It is important to note, however, that (i) this compensation may not occur in other regions and under different global climate conditions and (ii) that the RDM and GCM $\delta^{18}O_p$ have very different implications for interpreting paleoaltimetry. The RDM simulates very low $\delta^{18}O_p$ matching the proxy data (with values of $-21.5‰$) only at high elevations $\geq 4000$ m of NHL (fig. 7A, unfilled diamonds and cross mark). In contrast, the GCM simulates these low values over a range of elevations at NHL and also CHL, starting as low as 2000 m and extending to >4000 m (figs. 7A-7B, filled circles). The GCM results imply that elevations of the NHL and CHL inferred from the proxy $\delta^{18}O_p$ could have been lower than suggested by the *SWEEP* model. Additional GCM experiments are needed to explore this possibility.

On the eastern flank of the highlands, formation of convective precipitation, vapor recycling, and variability of moisture source substantially influence $\delta^{18}O_p$ (table 2). RDM models are known to severely underestimate (simulate values that are too negative) $\delta^{18}O_p$ on the leeside of mountain ranges. In agreement, our RDM with a GCM-moisture sources simulates $\delta^{18}O_p$ that is very low and substantially lower than that from the GCM (figs. 7D-7F, cross marks), a difference which we attribute to neglect of convective processes and vapor recycling, both of which enrich vapor and precipitation in $^{18}O$. In contrast, our RDM with a fixed moisture source simulates $\delta^{18}O_p$ that is higher and in good agreement with that from the GCM (figs. 7D-7E). This result is entirely due to the prescription in the RDM of a relatively enriched vapor source and high humidity and should not inspire much confidence in the RDM.

ECHAM5-wiso simulates $\delta^{18}O_p$ that is in good agreement with mineral $\delta^{18}O_p$ on the eastern slopes of CHL (fig. 7E) but is too high on the eastern slopes of SHL by ~2 to 3 permil (fig. 7F). This mismatch may derive from several causes presumably, as indicated by good agreement between RDM and mineral $\delta^{18}O_p$ (fig. 7E), not related to the vapor source. Counter to intuition, it may indicate that SHL elevations are too high, blocking flow over the highland and limiting vapor mixing between the eastern and the western air masses (fig. 4P). In support of this interpretation, we note that minimum $\delta^{18}O_p$ on the western flank of SHL is lower ($-18‰$, fig. 7E) by approximately 4 permil than that on the eastern flank. Alternatively, the mismatch may indicate too vigorous vapor recycling and/or monsoonal circulation on the eastern slopes. If this is the case, good agreement between GCM and proxy $\delta^{18}O_p$ over the CHL eastern slopes suggest that the bias is not systematic.

### *Caveats*

The GCM simulations presented here are sensitivity experiments that were conducted to explore the effect of surface topographic evolution on $\delta^{18}O_p$ and regional circulation and precipitation processes. They do not capture other important environmental changes that are known to have occurred in the early Cenozoic including Eocene to Oligocene global cooling and the initiation of Antarctic glaciation associated with carbon dioxide drawdown (for example, Barker and others, 2007);

and, regional and global changes in paleogeography, including the retreat of the Mississippian embayment (for example, Galloway and others, 2011), and filling of Laramide foreland basins (Dickinson and others, 1988). Paleoclimate modeling studies have shown that changes in atmospheric $CO_2$ and paleogeography can substantially influence climate and precipitation $\delta^{18}O$ over the South American Andes, while the influence of Antarctic glaciation is relatively minor (Jeffery and others, 2012; Poulsen and Jeffery, 2011).

In light of these studies, we suggest that $CO_2$ drawdown and infilling of the Mississippian Embayment and Laramide foreland basins probably had the most significant influences on $\delta^{18}O_p$ of the North American Cordillera. These events accelerated in the Late Eocene and early Oligocene and, as a consequence, would have mainly influenced $\delta^{18}O_p$ and paleoelevation interpretations associated with the SHL in the following ways: 1. The decrease of $CO_2$ from 1120 to 560 ppm would lead to a decrease of $\delta^{18}O_p$ due to downward mixing of more $^{18}O$-depleted moisture as a response to tropospheric cooling (Poulsen and Jeffery, 2011). 2. Global cooling may have favored snowfall at high elevations, contributing to lower $\delta^{18}O$ at the western flank. 3. Retreat of the Mississippian embayment potentially reduced transport of $^{18}O$-enriched moisture to the eastern flank of the highlands. 4. The infilling of the Laramide Basins and more frequent incursion of dry air masses from the Arctic due to an increased equator-to-pole temperature gradient may have increased aridity at the Laramide Foreland, as documented by paleofloras (Wing and Greenwood, 1993; Wolfe, 1994), and intensified a rain shadow along the eastern flank of the highlands. Taken together, climate change and regional geographic adjustments would have led to a decrease in $\delta^{18}O_p$, which have not been considered in either our GCM simulations or in paleoaltimetry reconstructions. Nonetheless, these influences and others discussed in Chamberlain and others (2012) would have been secondary to the large $\delta^{18}O_p$ depletion due to southward highland propagation.

### Implications for the SWEEP Model and Paleo-North American Monsoon

Our simulations show a north to south decrease in $\delta^{18}O_p$ in response to surface uplift that is consistent with the proxy $\delta^{18}O_p$ used to infer the *SWEEP* model (Mix and others, 2011; Chamberlain and others, 2012). Data model mismatches at several locations (figs. 6B and 6D) indicate the likelihood for requiring modest adjustments to the *SWEEP* topography, including lowering the interior of the northern Cordillera and the eastern flank of the southern Cordillera. While our simulations are consistent with (and in this way support) the *SWEEP* hypothesis, we cannot discount the feasibility of other tectonic models without additional simulations.

Both proxy data and climate models suggest the existence of a paleo-North American monsoon in the Cretaceous and Paleocene (for example, Poulsen and others, 1999; Sewall and Sloan, 2006; Fricke and others, 2010; Chamberlain and others, 2012). Paleoclimate models indicate that the Western Interior Seaway and, later, the Mississippian embayment may have been crucial to the land-ocean thermal contrast that drove the monsoon, and that as these water bodies retreated, both the strength and extent of the summer monsoon waned. In the Cretaceous, monsoonal circulation may have extended into Alberta (Poulsen and others, 1999; Fricke and others, 2010), but was mainly constrained to the eastern flank of the Rocky Mountain front in the early Paleogene (Sewall and Sloan, 2006). Topography has also been cited as an important inhibitor of the Eocene monsoon. In particular, Chamberlain and others (2012) speculate that the southward propagation of high topography in the Eocene blocked monsoonal transport of moisture into the northern and central Basin and Range.

Our simulations confirm the absence of monsoonal penetration into the Basin and Range (fig. 4M), but indicate that topographic growth is not the primary reason.

In the absence of an extensive embayment, strong westerly flow prevails over this region regardless of topographic scenario (figs. 4M-4O). Rather, our results suggest that the paleo-North American monsoon may have been somewhat rejuvenated by topographic migration. In response to uplift of the SHL, summer flow transports moisture from the Gulf of Mexico and intensifies summer precipitation along the eastern slopes of the Cordillera (figs. 4O and 4P).

<div align="center">CONCLUSIONS</div>

Our analysis using an isotope-enabled GCM supports stable isotopic evidence for Cenozoic southward propagation of high topography in the North American Cordillera and highlights the need to use caution in applying traditional $\delta^{18}O_p$ lapse rate-elevation relationships and open-system Rayleigh distillation models (RDM) to infer paleoelevations. Our analysis demonstrates significant contributions to $\delta^{18}O_p$ due to changes in precipitation phase and type, vapor mixing and recycling, and moisture sources at the windward and leeward side of the Cordillera in response to the growth and propagation of high topography. These processes lead to $\delta^{18}O_p$ variations that are different and sometimes opposite of those estimated using Rayleigh distillation models of moist adiabatic condensation.

Changes in $\delta^{18}O_p$ with uplift and propagation of topography are regionally variable and linked to process. On the windward western slopes of highlands, snow condensation and vapor mixing contribute substantially to precipitation $\delta^{18}O_p$ at high elevations of the northern and central cordillera. Snow condensation and contributions from a more subtropical moisture source dominate changes in precipitation $\delta^{18}O_p$ at the southern cordillera. The isotopic compensation of these processes disguises the isotopic signature of individual processes, causing GCM-simulated $\delta^{18}O_p$ to be similar to RDM $\delta^{18}O_p$ at the top of the highlands. On the eastern slopes, the moisture sources are different from and more $^{18}O$-depleted relative to the western slopes by $-2$ to $-4$ permil in the northern and central cordillera. These isotopic effects are muted by $^{18}O$-enrichment from both evaporative recycling and convective precipitation. At the southern cordillera, however, the moisture source is isotopically similar to the western flank due to moisture contributions from the paleo-Gulf of Mexico. As a result, GCM-simulated $\delta^{18}O_p$ is higher (less negative) than proxy $\delta^{18}O_p$. We suggest that due to partially blocking westward flow and limited zonal mixing, counter to intuition this mismatch may indicate that the *SWEEP* topography is too high.

Our examination of the isotopic signatures of precipitation processes indicates that these processes cannot be ignored in paleoaltimetry studies of the North American Cordillera. Similar processes are very likely to be important in other mountain belts as well and have evolved with surface uplift and regional climate change, altering local $\delta^{18}O_p$ patterns and lapse rates.

<div align="center">APPENDICES</div>

<div align="center">APPENDIX A: 1-D RAYLEIGH DISTILLATION MODEL OF ADIABATIC CONDENSATION (RDM)</div>

The RDM model is similar in concept to the model outlined in Rowley and Garzione (2007) for tracking a single near-surface air parcel along ascending, precipitating trajectories. The model is based on the conservation of moist static energy and tracks an unsaturated, ascending air parcel. The air parcel cools at the dry adiabatic lapse rate (K km$^{-1}$),

$$\Gamma_d = \frac{g}{c_p} \tag{1}$$

where g is the gravitational acceleration (ms$^{-2}$) and $c_p$ is the specific heat of dry air (J kg$^{-1}$K$^{-1}$), until it reaches the lifting condensation level (LCL). The LCL is defined as the first level where the air parcel temperature is less than the dew point temperature. Above this level, the air parcel cools at the moist adiabatic lapse rate,

$$\Gamma_s = -\frac{dT}{dz} = \Gamma_d \frac{[1 + L_c q_s/RT]}{[1 + \varepsilon L_c^2 q_s/(c_p R T^2)]} \qquad (2)$$

where $L_c$ is the latent heat of condensation (J kg$^{-1}$); $q_s$ is the saturation mixing ratio (kg/kg); R is the gas constant (J K$^{-1}$kg$^{-1}$); T is the air parcel temperature (K), e is the ratio of the molecular weight of water to that of dry air (0.622); and z (m) is the air-parcel height (Horton, 2004). The $T - z$ curve is modeled with a 210 m interval. The saturated-mixing ratio $q_s$ at each level is calculated from the saturation vapor pressure (Bolton, 1980):

$$e_s = 6.112 \exp\left(\frac{17.67 T_c}{T_c + 243.5}\right). \qquad (3)$$

$T_c$ is the temperature in degree Celsius (other temperatures are in Kelvin) at the j$^{th}$ level. The saturation mixing ratio is calculated:

$$q_s = \frac{\varepsilon e_s}{p - e_s} \qquad (4)$$

with $p$, the pressure at the j$^{th}$ level, calculated:

$$p = p_{j-1}\left(\frac{T}{T_{j-1}}\right)^{\frac{g}{\Gamma_s R}}. \qquad (5)$$

$p_{j-1}$ and $T_{j-1}$ is the pressure and temperature at the (j-1)$^{th}$ level. For the j$^{th}$ level, the fractionation factor is calculated using Majoube (1971) for liquid-vapor equilibrium:

$$1000 \ln \alpha = -7.685 + \frac{6.7123 \times 10^3}{T} - \frac{1.6664 \times 10^3}{T^2} + \frac{0.35041 \times 10^9}{T^3}. \qquad (6)$$

The remaining vapor fraction f $= \dfrac{(e_s)_j}{(e_s)_{j-1}}$ is used to calculate the delta value of remaining vapor and condensation, using:

$$(\delta^{18}O_v)_j = ((\delta^{18}O_v)_{j-1} + 1000)f^{(\alpha - 1)} - 1000$$
$$(\delta^{18}O_l)_j = \alpha((\delta^{18}O_v)_j + 1000) - 1000 \qquad (7)$$

where $\delta^{18}O_v$ and $\delta^{18}O_l$ are the isotopic composition of the remaining vapor and condensation.

The RDM calculates the $\delta^{18}O_p$-elevation relationship with given surface air temperature ($T_s$), 1000 hPa specific humidity ($q_s$) and $\delta^{18}O_v$ at the first step. These three values determine the moisture source of the ascending air parcel. In this study, the moisture sources are prescribed as either *fixed* or from *GCM*. The *fixed-moisture source* has $\delta^{18}O_v$ inferred from mineral $\delta^{18}O_p$ (−9.9 permil, based on the isotopic composition of kaolinitized Eocene river gravel deposited in the ancestral Yuba River near the ancient Pacific shoreline (Mulch and others, 2006)) and $T_s$, and $q_s$ taken from the western side of the highlands of a GCM simulation. The *GCM-moisture source* is initiated with $\delta^{18}O_v$, $T_s$, and $q_s$ from a GCM simulation. GCM variables are prescribed on either the western or eastern sides of the highlands.

For both *fixed- and GCM-moisture sources*, the initial values of $\delta^{18}O_v$ is derived from $\delta^{18}O_p$ of initial condensations either from fixed $\delta^{18}O_p$ of −9.9 permil or $\delta^{18}O_p$ of GCM condensates, because $\delta^{18}O_v$ varies substantially at low levels (for example, from −16.2‰ to −21.4‰ between 1000 and 850 hPa over a domain of 53°±2° N, 125° W). We select an appropriate $\delta^{18}O_v$ by first running the RDM with the full range of low-level $\delta^{18}O$ values with given $T_s$ and $q_s$. We then choose the initial $\delta^{18}O_v$ that best matches the fixed or GCM (≤1200 m) $\delta^{18}O_p$ of initial condensations along the mountain slopes of NHL, CHL, and SHL.

$T_s$, $q_s$, and $\delta^{18}O_v$ are taken at 125° W for a western moisture source for NHL, CHL and SHL scenarios, at 90° W for an eastern moisture source in NHL and CHL scenarios and at 95° W in the SHL scenario. Both $T_s$ and $q_s$ are averaged across a small range of latitudes encompassing the highlands (which are NHL, 57°±3° N; CHL, 53°±2° N; SHL, 47°±4° N).

The RDM is modified to consider vapor input due to expansion of the air parcel in response to both adiabatic and non-adiabatic heating of the environmental atmosphere along the eastern flanks of the mountains. On the leeside of the North American Cordillera, the (environmental) atmosphere is warmer than its surroundings at the same elevations due to non-adiabatic heating through large-scale subsidence and the release of latent heat from convective condensates. The ascending air parcels at the leeside of the mountains are diabatically warmed by the warmer environmental atmosphere, which leads to additional expansion and enhanced water-holding capacity of ascending air parcels. This effect is approximated by increasing the mixing ratio at each level of calculation assuming isothermal expansion of the air mass and that the added vapor has the same isotopic composition as the existing vapor. At each step above the LCL, $q_s$, $\delta^{18}O_v$, $\delta^{18}O_p$, T are first calculated from equations (1) through (7), and then $q_s$ is adjusted to include the vapor recycling potential r (the ratio of evaporation to precipitation): $q_s = q_s \times (1+r)$. This modification is included to approximate the re-evaporation process.

Back trajectory analysis of air parcels is commonly performed along isentropic (that is uniform potential temperature) surfaces to analyze the origin and path of precipitation (for example, Dirmeyer and Brubaker, 1999). However, in regions of active thermal convection and strong diabatic heating, conditions that are prevalent on the eastern side of the Eocene North American Cordillera, potential temperature is not conserved and flow. Non-isentropic transport of moisture could also be inferred at the western flank as extensive moisture mixing across different altitude is generated by mountain waves.

With these considerations, instead of using strict isentropic tracking, we track bulk moisture in the boundary layer (1000 to 850 hPa) where moisture is concentrated. The horizontal location of a parcel (x, y) is given in explicit form by (Kurita and others, 2004):

$$x^{n+1} = x^n + \int_t^{t+\Delta t} u^*(x, y, t)\, dt$$

$$y^{n+1} = y^n + \int_t^{t+\Delta t} v^*(x, y, t)\, dt$$

where u* and v* are zonal and meridional winds weighted by the boundary layer profile of relative humidity. The vertical average (850-1000 hPa) of relative humidity is also recorded at (x, y). We report the back trajectories for parcels that arrive the target location with high relative humidity ($\geq 60\%$) to filter dry parcels that have little potential for precipitation.

TABLE D1

$\delta^{18}O_p$ *values summarized from other studies and calculated from reported mineral* $\delta^{18}O$ *using inferred paleoflora proxy temperature (Mix and others, 2011; Chamberlain and others, 2012) and recalculated* $\delta^{18}O_p$ *value using model temperature by this study*

| Region | Lat | Lon | Age | Temperature (°C) | $\delta^{18}O_p$ | Model Surface Temperature ($T_s$, °C) | $\delta^{18}O_p$ using Model $T_s$ |
|---|---|---|---|---|---|---|---|
| pre-49Ma | | | | | | | |
| Axehandle_Basin_(UT) | 39.41 | -111.7 | 55 | 22 (1) | -6.7 | 20.4 | -7.1 |
| Axehandle_Basin_(UT) | 39.4 | -111.68 | 71.3-50 | 16.9 (1) | -8.3 | 20.4 | -8.1 |
| Bannock_Basin_(ID) | 42.09 | -112.18 | 50-49 | 12.5 (2) | -14.3 | 18.3 | -13.0 |
| Bighorn_Basin_(WY) | 45 | -109 | 57.7-53.2 | 16 (2) | -7.8 | 18.0 | -7.5 |
| Bighorn_Basin_(WY) | 44 | -108.8 | 58.8-53.6 | | -10.3 | * | |
| Bighorn_Basin_(WY) | 44.84 | -108.84 | 55.8 | 16.5 (2) | -7.9 | 18.0 | -8.0 |
| Bighorn_Basin_(WY) | 42.22 | -108.53 | 50.8-51.9 | 17.5 (2) | -7.1 | 21.1 | -7.4 |
| Crazy_Mtn_Basin_(MT) | 46.4 | -110.2 | 64.4-59.4 | | -13.8 | * | |
| Elko_Basin_(NV) | 40.56 | -116.01 | 54.5-49.0 | 21.5 (2) | -4 | 18.6 | -4.6 |
| Flagtaff_Basin_(UT) | 39 | -110.5 | 55 | 22 (1) | -7 | 21.1 | -7.3 |
| Great_Plains/Rocky_Mts | 43.83 | -108.55 | 50 | 10.9 (2) | -11.8 | 19.8 | -9.9 |
| Greater_Green_River_Basin_(WY) | 40.76 | -108.89 | 51.8-52.0 | | -7.4 | * | |
| Greater_Green_River_Basin_(WY) | 41.5 | -109 | 53 | | -8 | * | |
| Greater_Green_River_Basin_(WY) | 41.5 | -109 | 54 | | -10.6 | * | |
| Greater_Green_River_Basin_(WY) | 41.5 | -109 | 51 | | -9.4 | * | |
| Greater_Green_River_Basin_(WY) | 41.75 | -108.8 | 49 | 17.2 (1) | -2.7 | 21.3 | -2.1 |
| Greater_Green_River_Basin_(WY) | 41.5 | -109.5 | 52 | 17.2 (1) | -1.4 | 20.8 | -0.9 |
| Okanagan_Kettle_MCC_(WA) | 48.5 | -118.25 | 49.1 | | -13.3 | * | -13.3 |
| Piceance_Creek_Basin_(CO) | 39.41 | -108.18 | 52 | 22 (1) | -8.4 | 20.9 | -8.7 |
| Powder_River_Basin_(WY) | 45.5 | -106 | 53.7-57.3 | | -13.7 | * | |
| Princeton_Basin_(BC) | 49.44 | -120.5 | 49 | 8.3 (1) | -19.7 | 3.7 | -21.5 |
| Sage_Creek_Basin_(MT/ID) | 44.74 | -112.61 | 65-49 | 11-16 (2) | -8.4 | 17.7 | -7.5 |
| Shuswap_MCC_(BC) | 51 | -118.25 | 49.0-47.9 | | -15.8 | * | |
| Uinta_Basin_(UT) | 39.81 | -110.94 | 55 | 22 (1) | -9.8 | 20.3 | -10.2 |
| Wind_River_Range_(WY) | 43.24 | -107.5 | 52.8-52.0 | 16.5 (2) | -13.6 | 20.0 | -12.8 |
| Wind_River_Range_(WY) | 43.33 | -107.63 | 53.2-52.7 | 17.5 (2) | -12.6 | 20.0 | -11.9 |
| Wind_River_Range_(WY) | 43.49 | -109.45 | 55.5-53.2 | 19.8 (2) | -8.5 | 19.2 | -8.8 |
| Wind_River_Range_(WY) | 43.02 | -107.08 | 60-55 | 21.5 (2) | -9.3 | 20.0 | -9.7 |
| Wind_River_Range_(WY) | 43.22 | -107.3 | 52-50.9 | 16.5 (2) | -13.9 | 20.0 | -13.1 |
| 49-39Ma | | | | | | | |
| Bannock_Basin_(ID) | 42.09 | -112.18 | 48-41 | 12.3 (2) | -12.3 | 16.3 | -11.4 |
| Elko_Basin_(NV) | 40.56 | -116.02 | 47.5-39.4 | 15.8 (2) | -6.7 | 19.0 | -7.1 |
| Elko_Basin_(NV) | 40.58 | -115.99 | 42.6-40.6 | 12.4 (2) | -4.1 | 19.0 | -3.0 |
| Flagstaff_Basin_(UT) | 38.92 | -111.81 | 49-39 | 13.2 (2) | -8.7 | 20.6 | -7.3 |
| Galisteo_Basin_(NM) | 35.5 | -106 | 49-39 | 7.5 (2) | -10 | 24.5 | -6.4 |
| Great_Plains/Rocky_Mts | 43.5 | -108.58 | 47.9 | 10 (2) | -12.9 | 18.5 | -11.1 |
| Great_Plains/Rocky_Mts | 42.76 | -107.59 | 49 | 10.9 (2) | -13.4 | 20.8 | -11.3 |
| Great_Plains/Rocky_Mts | 42.71 | -108.18 | 49 | 10.9 (2) | -13.2 | 20.8 | -11.1 |
| Great_Plains/Rocky_Mts | 42.6 | -108.29 | 49 | 10.9 (2) | -11.9 | 20.6 | -9.9 |
| Great_Plains/Rocky_Mts | 44.85 | -110.16 | 49 | 10.9 (2) | -18.5 | 15.7 | -17.3 |
| Great_Plains/Rocky_Mts | 44.87 | -111.05 | 49 | 10.9 (2) | -17.4 | 12.5 | -16.9 |
| Great_Plains/Rocky_Mts | 44.89 | -111.33 | 49 | 10.9 (2) | -18.1 | 12.5 | -17.6 |
| Greater_Green_River_Basin_(WY) | 41.75 | -108.8 | 48 | 17.2 (1) | -7.2 | 21.7 | -6.4 |

TABLE D1

*(continued)*

| Region | Lat | Lon | Age | Temperature (°C) | $\delta^{18}O_p$ | Model Surface Temperature ($T_s$, °C) | $\delta^{18}O_p$ using Model $T_s$ |
|---|---|---|---|---|---|---|---|
| 49-39Ma | | | | | | | |
| Ibapah_Basin (UT) | 40.12 | -114.12 | 46-39 | 13.2 (2) | -10.8 | 19.4 | -9.5 |
| Sage_Creek_Basin (MT/ID) | 44.66 | -112.58 | 48.0-39.1 | 13.4 (2) | -17.1 | 7.3 | -18.2 |
| Sierra_Nevada (CA) | 39.35 | -120.98 | 44.9 | | -9.3 | * | |
| Sierra_Nevada (CA) | 39.18 | -120.85 | 44.9 | | -10.1 | * | |
| Sierra_Nevada (CA) | 39.69 | -120.93 | 44.9 | | -10 | * | |
| Sierra_Nevada (CA) | 39.69 | -120.98 | 44.9 | | -9.8 | * | |
| Uinta_Basin (UT) | 40.05 | -110.53 | 49-39 | 13.2 (2) | -3.6 | 20.5 | -2.3 |
| 39-28Ma | | | | | | | |
| Claron_Basin (UT) | 37.68 | -112.83 | 39-28 | 11 (2) | -16.3 | 8.0 | -16.8 |
| Copper_Basin (NV) | 41.76 | -115.47 | 38.7 | 10.5 (1) | -18.2 | 7.0 | -18.7 |
| Elko_Basin (NV) | 40.55 | -115.96 | 36.0-28.0 | 13 (2) | -16.1 | 8.5 | -17.0 |
| Flastaff_Basin (UT) | 38.93 | -111.95 | 39-28 | 11 (2) | -15.7 | 6.9 | -16.5 |
| Galisteo_Basin (NM) | 35.5 | -106 | 39-28 | 0 (2) | -11.8 | 24.1 | -6.6 |
| Great_Plains/Rocky_Mts | 42.83 | -101.7 | 35 | 11.5 (2) | -9.8 | 17.3 | -8.6 |
| Great_Plains/Rocky_Mts | 43.66 | -102.66 | 35.8 | 11.5 (2) | -8.1 | 17.0 | -7.0 |
| Great_Plains/Rocky_Mts | 41.6 | -103.11 | 31.25 | 11.5 (2) | -9.2 | 18.2 | -7.9 |
| Great_Plains/Rocky_Mts | 41.7 | -103.34 | 31.25 | 11.5 (2) | -8.6 | 18.2 | -7.2 |
| Great_Plains/Rocky_Mts | 42.92 | -103.49 | 34.5 | 11.5 (2) | -10.6 | 17.5 | -9.3 |
| Great_Plains/Rocky_Mts | 42.77 | -103.56 | 30.3 | 11.5 (2) | -10.5 | 17.5 | -9.2 |
| Great_Plains/Rocky_Mts | 42.76 | -105.01 | 35.5 | 11.5 (2) | -10.9 | 17.8 | -9.6 |
| Great_Plains/Rocky_Mts | 42.71 | -105.37 | 31.25 | 11.5 (2) | -12.8 | 17.8 | -11.4 |
| Great_Plains/Rocky_Mts | 42.64 | -106.76 | 35.65 | 11.5 (2) | -13.3 | 19.2 | -11.7 |
| Great_Plains/Rocky_Mts | 42.76 | -107.56 | 32 | 11.5 (2) | -16.6 | 20.3 | -14.6 |
| Great_Plains/Rocky_Mts | 42.58 | -108.29 | 32 | 11.5 (2) | -16.9 | 19.1 | -15.2 |
| Sage_Creek_Basin (MT/ID) | 44.76 | -112.55 | 38.8-32.0 | 10.8 (2) | -17 | 2.8 | -18.7 |
| Sierra_Nevada (CA) | 39.7 | -120.99 | 28.5 | | -14.3 | * | |
| Sierra_Nevada (CA) | 39.85 | -120.35 | 28.5 | | -16.8 | * | |
| Sierra_Nevada (CA) | 39.25 | -120.93 | 28.5 | | -13.2 | * | |
| Sierra_Nevada (CA) | 39.46 | -120.49 | 28.5 | | -15.3 | * | |
| Sierra_Nevada (CA) | 39.56 | -120.5 | 28.5 | | -16.2 | * | |
| Sierra_Nevada (CA) | 38.19 | -120.85 | 28.5 | | -10.6 | * | |
| Uinta_Basin (UT) | 40.33 | -109.53 | 39-28 | 11 (2) | -13.4 | 13.9 | -12.7 |
| Wind_River_Range (WY) | 42.7 | -108.19 | 36.8-28.3 | 11.3 (2) | -14.1 | 17.1 | -12.9 |
| Wind_River_Range (WY) | 43.34 | -107.48 | 37.0-34.0 | 11.5 (2) | -11.1 | 15.8 | -10.2 |

(1) Wolfe and others, 1997.
(2) Chase and others, 1998.
* Used reported $\delta^{18}O$ as $\delta^{18}O_p$.

REFERENCES

Andreasson, F. P., and Schmitz, B., 1998, Tropical Atlantic seasonal dynamics in the Early Middle Eocene from stable oxygen and carbon isotope profiles of mollusk shells: Paleoceanography, v. 13, n. 2, p. 183–192, http://dx.doi.org/10.1029/98PA00120

———— 2000, Temperature seasonality in the early middle Eocene North Atlantic region: Evidence from stable isotope profiles of marine gastropod shells: Geological Society of America Bulletin, v. 112, n. 4, p. 628–640, http://dx.doi.org/10.1130/0016-7606(2000)112⟨628:TSITEM⟩2.0.CO;2

Barker, P. F., Diekmann, B., and Escutia, C., 2007, Onset of Cenozoic Antarctic glaciation: Deep-Sea Research II, v. 54, n. 21–22, p. 2293–2307, http://dx.doi.org/10.1016/j.dsr2.2007.07.027

Beerling, D. J., and Royer, D. L., 2011, Convergent Cenozoic $CO_2$ history: Nature Geoscience, v. 4, p. 418–420, http://dx.doi.org/10.1038/ngeo1186

Bice, K. L., Scotese, C. R., Seidov, D., and Barron, E. J., 2000, Quantifying the role of geographic change in Cenozoic ocean heat transport using uncoupled atmosphere and ocean models: Palaeogeography, Palaeoclimatology, Palaeoecology, v. 161, n. 34, p. 295–310, http://dx.doi.org/10.1016/S0031-0182(00)00072-9

Blisniuk, P. M., and Stern, L. A., 2005, Stable isotope paleoaltimetry: A critical review: American Journal of Science, v. 305, n. 10, p. 1033–1074, http://dx.doi.org/10.2475/ajs.305.10.1033

Bolton, D., 1980, The computation of equivalent potential temperature: Monthly Weather Review, v. 108, p. 1046–1053, http://dx.doi.org/10.1175/1520-0493(1980)108⟨1046:TCOEPT⟩2.0.CO;2

Bowen, G. J., Daniels, A. D., and Bowen, B. B., 2008, Paleoenvironmental isotope geochemistry and paragenesis of lacustrine and palustrine carbonates, Flagstaff Formation, Central Utah, U.S.A.: Journal of Sedimentary Research, v. 78, n. 3, p. 162–174, http://dx.doi.org/10.2110/jsr.2008.021

Bown, T. M., and Kraus, M. J., 1981, Lower Eocene alluvial paleosols (Willwood Formation, Northwest Wyoming, U.S.A.) and their significance for paleoecology, palcoclimatology and basin analysis: Palaeogeography, Palaeoclimatology, Palaeoecology, v. 34, p. 1–30, http://dx.doi.org/10.1016/0031-0182(81)90056-0

Brinkhuis H., Schouten, S., Collinson, M. E., Sluijs, A., Sinninghe-Damsté, J. S., Dickens, G. R., Huber, M., Cronin, T. M., Onodera, J., Takahashi, K., Bujak, J. P., Stein, R., van der Burgh, J., Eldrett, J. S., Harding, I. C., Lotter, A. F., Sangiorgi, F., van Konijnenburg-van Cittert, H., de Leeuw, J. W., Matthiessen, J., Backman, J., Moran, K., and the Expedition 302 Scientists, 2006, Episodic fresh surface waters in the Eocene Arctic Ocean: Nature, v. 441, p. 606–609, http://dx.doi.org/10.1038/nature04692

Chamberlain, C. P., Mix, H. T., Mulch, A., Hren, M. T., Kent-Corson, M. L., Davis, S. J., Horton, T. W., and Graham, S. A., 2012, The Cenozoic climatic and topographic evolution of the Western North America Cordillera: American Journal of Science, v. 312, n. 2, p. 213–262, http://dx.doi.org/10.2475/02.2012.05

Chase, C. G., Gregory-Wodzicki, K. M., Parrish-Jones, J. T., and DeCelles, P. G., 1998, Topographic history of the western Cordillera of North America and controls on climate, *in* Crowley, T. J., and Burke, K., editors, Tectonic boundary conditions for climate model simulations: New York, Oxford University Press, Oxford Monographs on Geology and Geophysics, p. 73–99.

Clark, M. K., 2007, The significance of paleotopography: Reviews in Mineralogy and Geochemistry, v. 66, n. 1, p. 1–21, http://dx.doi.org/10.2138/rmg.2007.66.1

Clementz, M. T., and Sewall, J. O., 2011, Latitudinal gradients in greenhouse seawater $\delta^{18}O$: Evidence from Eocene Sirenian tooth enamel: Science, v. 332, n. 6028, p. 455–458, http://dx.doi.org/10.1126/science.1201182

Cook, K. H., Edward, E. K., Launer, Z. S., and Patricola, C. M., 2008, Springtime intensification of the Great Plains low-level jet and Midwest precipitation in GCM simulations of the twenty-first century: Journal of Climate, v. 21, p. 6321–6340, http://dx.doi.org/10.1175/2008JCLI2355.1

Davis, S. J., Mix, H. T., Wiegand, B. A., Carroll, A. R., and Chamberlain, C. P., 2009, Synorogenic evolution of large-scale drainage patterns: Isotope paleohydrology of sequential Laramide basins: American Journal of Science, v. 309, n. 7, p. 549–602, http://dx.doi.org/10.2475/07.2009.02

DeCelles, P. G., 2004, Late Jurassic to Eocene evolution of the Cordilleran thrust belt and foreland basin system, western USA: American Journal of Science, v. 304, n. 2, p. 105–168, http://dx.doi.org/10.2475/ajs.304.2.105

Dettman, D. L., and Lohmann, K. C., 2000, Oxygen isotope evidence for high-altitude snow in the Laramide Rocky Mountains of North America during the Late Cretaceous and Paleogene: Geology, v. 28, n. 3, p. 243–246, http://dx.doi.org/10.1130/0091-7613(2000)28⟨243:OIEFHS⟩2.0.CO;2

Dickinson, W. R., 2004, Evolution of the North American cordillera: Annual Review of Earth and Planetary Sciences, v. 32, p. 13–45, http://dx.doi.org/10.1146/annurev.earth.32.101802.120257

Dickinson, W. R., Klute, M. A., Hayes, M. J., Janecke, S. U., Lundin, E. R., McKittrick, M. A., and Olivares, M. D., 1988, Paleogeographic and paleotectonic setting of Laramide sedimentary basins in the central Rocky Mountain region: Geological Society of America Bulletin, v. 100, n. 7, p. 1023–1039, http://dx.doi.org/10.1130/0016-7606(1988)100⟨1023:PAPSOL⟩2.3.CO;2

Dirmeyer, P. A., and Brubaker, K. L., 1999, Contrasting evaporative moisture sources during the drought of 1988 and the flood of 1993: Journal of Geophysical Research—Atmospheres, v. 104, n. D16, p. 19383–19397, http://dx.doi.org/10.1029/1999JD900222

Ehlers, T. A., and Poulsen, C. J., 2009, Influence of Andean uplift on climate paleoaltimetry estimates: Earth and Planetary Science Letters, v. 281, n. 3–4, p. 238–248, http://dx.doi.org/10.1016/j.epsl.2009.02.026

Forte, A. M., Moucha, R., Simmons, N. A., Grand, S. P., and Mitrovica, J. X., 2010, Deep-mantle contributions to the surface dynamics of the North American continent: Tectonophysics, v. 481, n. 1–4, p. 3–15, http://dx.doi.org/10.1016/j.tecto.2009.06.010

Frankenberg, C., Yoshimura, K., Warneke, T., Aben, I., Butz, A., Deutscher, N., Griffth, D., Hase, F., Notholt,

J., Schneider, M., Schrijver, H., and Roeckmann, T., 2009, Dynamic Processes Governing Lower-Tropospheric HDO/H$_9$O ratios as observed from space and ground: Science, v. 325, n. 5946, p. 1374–1377, http://dx.doi.org/10.1126/science.1173791

Fricke, H. C., 2003, Investigation of early Eocene water-vapor transport and paleoelevation using oxygen isotope data from geographically widespread mammal remains: Geological Society of America Bulletin, v. 115, n. 9, p. 1088–1096, http://dx.doi.org/10.1130/B25249.1

Fricke, H. C., and Wing, S. L., 2004, Oxygen isotope and paleobotanical estimates of temperature and δ$^{18}$O-latitude gradients over North America during the early Eocene: American Journal of Science, v. 304, n. 7, p. 612–635, http://dx.doi.org/10.2475/ajs.304.7.612

Fricke, H. C., Foreman, B. Z., and Sewall, J. O., 2010, Integrated climate model-oxygen isotope evidence for a North American monsoon during the Late Cretaceous: Earth and Planetary Science Letters, v. 289, p. 11–21, http://dx.doi.org/10.1016/j.epsl.2009.10.018

Galewsky, J., 2009, Orographic precipitation isotopic ratios in stratified atmospheric flows: Implications for paleoelevation studies: Geology, v. 37, n. 9, p. 791–794, http://dx.doi.org/10.1130/G30008A.1

Galloway, W. E., Whiteaker, T. L., and Ganey-Curry, P., 2011, History of Cenozoic North American drainage basin evolution, sediment yield, and accumulation in the Gulf of Mexico basin: Geosphere, v. 7, n. 4, p. 938–973, http://dx.doi.org/10.1130/GES00647.1

Garzione, C. N., Molnar, P., Libarkin, J. C., and MacFadden, B. J., 2006, Rapid late Miocene rise of the Bolivian Altiplano: Evidence for removal of mantle lithosphere: Earth and Planetary Science Letters, v. 241, n. 3–4, p. 543–556, http://dx.doi.org/10.1016/j.epsl.2005.11.026

Gat, J. R., 2010, Snow and snowmelt processes, *in* Gat, J. R., Isotope Hydrology: A Study of the Water Cycle: World Scientific, p. 67–69, http://dx.doi.org/10.1142/9781848164741_0007

Gat, J. R., and Rietti-Shati, M., 1999, The meteorological vs. the hydrological altitude effect on the isotopic composition of meteoric waters, *in* IAEA-CSP2/C, editors, Isotope techniques in water resources development and management: IAEA-Symposium, paper n. SM-361/2.

Gedzelman, S. D., 1988, Deuterium in water vapor above the atmospheric boundary layer: Tellus B, v. 40, n. 2, p. 134–147, http://dx.doi.org/10.1111/j.1600-0889.1988.tb00217.x

Greenwood, D. R., and Wing, S. L., 1995, Eocene continental climates and latitudinal temperature-gradients: Geology, v. 23, p. 1044–1048, http://dx.doi.org/10.1130/0091-7613(1995)023⟨1044:ECCALT⟩2.3.CO;2

Hagemann, S., 2002, An improved land surface parameter dataset for global and regional climate models: Max Planck Institute for Meteorology, Report No. 336, p. 21.

Heinemann, M., Jungclaus, J. H., and Marotzke, J., 2009, Warm Paleocene/Eocene climate as simulated in ECHAM5/MPI-OM: Climate of the Past, v. 5, p. 785–802, http://dx.doi.org/10.5194/cp-5-785-2009

Hoffmann, G., Werner, M., and Heimann, M., 1998, Water isotope module of the ECHAM atmospheric general circulation model—A study on timescales from days to several years: Journal of Geophysical Research, v. 103, n. D14, p. 16871–16896, http://dx.doi.org/10.1029/98JD00423

Hoffmann, G., Jouzel, J., and Masson, V., 2000, Stable water isotopes in atmospheric general circulation models: Hydrological Processes, v. 14, n. 8, p. 1385–1406, http://dx.doi.org/10.1002/1099-1085 (20000615)14:8⟨1385::AID-HYP989⟩3.0.CO;2-l

Holton, J. R., 2004, Moisture variables, *in* An introduction to dynamic meteorology: Waltham, Massachusetts, Academic press, p. 503.

Horton, T. W., Sjostrom, D. J., Abruzzese, M. J., Poage, M. A., Waldbauer, J. R., Hren, M., Wooden, J., and Chamberlain, C. P., 2004, Spatial and temporal variation of the Cenozoic surface elevation in the Great Basin and Sierra Nevada: American Journal of Science, v. 304, n. 10, p. 862–888, http://dx.doi.org/10.2475/ajs.304.10.862

Humphreys, E. D., 1995, Post-Laramide removal of the Farallon slab, western United States: Geology, v. 23, n. 11, p. 987–990, http://dx.doi.org/10.1130/0091-7613(1995)023⟨0987:PLROTF⟩2.3.CO;2

Insel, N., Poulsen, C. J., and Ehlers, T. A., 2009, Influence of the Andes Mountains on South American moisture transport, convection, and precipitation: Climate Dynamics, v. 35, n. 7–8, p. 1477–1492, http://dx.doi.org/10.1007/s00382-009-0637-1

Insel, N., Poulsen, C. J., Ehlers, T. A., and Sturm, C., 2012, Response of meteoric δ$^{18}$O to surface uplift—Implications for Cenozoic Andean Plateau growth: Earth and Planetary Science Letters, v. 317–318, p. 262–272, http://dx.doi.org/10.1016/j.epsl.2011.11.039

Ivany, L. C., Lohmann, K. C., Hasiuk, F., Blake, D. B., Glass, A., Aronson, R. B., and Moody, R. M., 2008, Eocene climate record of a high southern latitude continental shelf: Seymour Island, Antarctica: Geological Society of America Bulletin, v. 120, n. 5–6, p. 659–678, http://dx.doi.org/10.1130/B26269.1

Jeffery, M. L., Poulsen, C. J., and Ehlers, T. A., 2012, Impacts of global cooling, surface uplift and an inland seaway on South American paleoclimate and precipitation δ$^{18}$O: Geological Society of America Bulletin, v. 124, n. 3–4, p. 335–351, http://dx.doi.org/10.1130/B30480.1

Jouzel, J., and Merlivat, L., 1984, Deuterium and oxygen-18 in precipitation: Modeling of the isotopic effects during snow formation: Journal of Geophysical Research—Atmospheres, v. 89, n. D7, http://dx.doi.org/10.1029/JD089iD07p11749

Kharin, V. V., Zwiers, F. W., Zhang, X., and Hegerl, G. C., 2007, Changes in temperature and precipitation extremes in the IPCC ensemble of global coupled model simulations: Journal of Climate, v. 20, p. 1419–1444, http://dx.doi.org/10.1175/JCLI4066.1

Koch, P. L., Zachos, J. C., and Dettman, D. L., 1995, Stable isotope stratigraphy and paleoclimatology of the Paleogene Bighorn Basin, (Wyoming, U.S.A.): Palaeogeography, Palaeoclimatology, Palaeoecology, v. 115, n. 1–4, p. 61–89, http://dx.doi.org/10.1016/0031-0182(94)00107-J

Kurita, N., Yoshida, N., Inoue, G., and Chayanova, E. A., 2004, Modern isotope climatology of Russia: A first assessment: Journal of Geophysical Research, v. 109, n. D031023, p. 1984–2012, http://dx.doi.org/10.1029/2003JD003404

Lechler, A. R., and Galewsky, J., 2013, Refining paleoaltimetry reconstructions of the Sierra Nevada, California, using air parcel trajectories: Geology, v. 41, n. 2, p. 259–262, http://dx.doi.org/10.1130/G33553.1

Lechler, A. R., and Niemi, N. A., 2011, Controls on the spatial variability of modern meteoric $\delta^{18}$O: Empirical constraints from the western US and east Asia and implications for stable isotope studies: American Journal of Science, v. 311, n. 8, p. 664–700, http://dx.doi.org/10.2475/08.2011.02

Majoube, M., 1971, Fractionnement en oxygen 18 et en deuterium entre l'eau et sa vapeur: Journal de Chimie et de Physique, v. 68, n. 10, p. 1423–1436.

Mix, H. T., Mulch, A., Kent-Corson, M. L., and Chamberlain, C. P., 2011, Cenozoic migration of topography in the North American Cordillera: Geology, v. 39, n. 1, p. 87–90, http://dx.doi.org/10.1130/G31450.1

Morrill, C., and Koch, P. L., 2002, Elevation or alteration? Evaluation of isotopic constraints on paleoaltitudes surrounding the Eocene Green River Basin: Geology, v. 30, n. 2, p. 151–154, http://dx.doi.org/10.1130/0091-7613(2002)030⟨0151:EOAEOI⟩2.0.CO;2

Moser, H., and Stichler, W., 1971, Die Verwendung des Deuterium- und Sauerstoff-18-Gehalts bei hydrologischen Untersuchungen: Geologica Bavaria, v. 64, p. 7–35.

Mulch, A., Graham, S. A., and Chamberlain, C. P., 2006, Hydrogen isotopes in Eocene river gravels and paleoelevation of the Sierra Nevada: Science, v. 313, n. 5783, p. 87–89, http://dx.doi.org/10.1126/science.1125986

Mulch, A., Teyssier, C., Cosca, M. A., and Chamberlain, C. P., 2007, Stable isotope paleoaltimetry of Eocene Core Complexes in the North American Cordillera: Tectonics, v. 26, n. 4, TC4001, http://dx.doi.org/10.1029/2006TC001995

Norris, R. D., Jones, L. S., Corfield, R. M., and Cartlidge, J. E., 1996, Skiing in the Eocene Uinta Mountains? Isotopic evidence in the Green River Formation for snow melt and large mountains: Geology, v. 24, n. 5, p. 403–403, http://dx.doi.org/10.1130/0091-7613(1996)024⟨0403:SITEUM⟩2.3.CO;2

Pearson, P. N., van Dongen, B. E., Nicholas, C. J., Pancost, R. D., Schouten, S., Singano, J. M., and Wade, B. S., 2007, Stable warm tropical climate through the Eocene Epoch: Geology, v. 35, n. 3, p. 211–214, http://dx.doi.org/10.1130/G23175A.1

Peppe, D. J., Royer, D. L., Wilf, P., and Kowalski, E. A., 2010, Quantification of large uncertainties in fossil leaf paleoaltimetry: Tectonics, v. 29, n. 3, TC3015, http://dx.doi.org/10.1029/2009TC002549

Pierrehumbert, R. T., 1998, Lateral mixing as a source of subtropical water vapor: Geophysical Research Letters, v. 25, n. 2, p. 151–154, http://dx.doi.org/10.1029/97GL03563

Pierrehumbert, R. T., and Yang, H., 1993, Global Chaotic Mixing on Isentropic Surfaces: Journal of Atmospheric Science, v. 50, n. 15, p. 2462–2480, http://dx.doi.org/10.1175/1520-0469(1993)050⟨2462:GCMOIS⟩2.0.CO;2

Poage, M. A., and Chamberlain, C. P., 2001, Empirical relationships between elevation and the stable isotope composition of precipitation and surface waters: considerations for studies of paleoelevation change: American Journal of Science, v. 301, n. 1, p. 1–15, http://dx.doi.org/10.2475/ajs.301.1.1

Poulsen, C. J., and Jeffery, M. L., 2011, Climate change imprinting on stable isotopic compositions of high-elevation meteoric water cloaks past surface elevations of major orogens: Geology, v. 39, n. 6, p. 595–598, http://dx.doi.org/10.1130/G32052.1

Poulsen, C. J., Barron, E. J., Johnson, C. C., and Fawcett, P., 1999, Links between major climatic factors and regional oceanic circulation in the mid-Cretaceous, *in* Barrera, E., and Johnson, C. C., editors, Evolution of the Cretaceous Ocean-Climate System: Geological Society of America Special Paper, v. 332, p. 73–89, http://dx.doi.org/10.1130/0-8137-2332-9.73

Poulsen, C. J., Ehlers, T. A., and Insel, N., 2010, Onset of convective rainfall during gradual Late Miocene rise of the Central Andes: Science, v. 328, n. 5977, p. 490–493, http://dx.doi.org/10.1126/science.1185078

Risi, C., Bony, S., and Vimeux, F., 2008, Influence of convective processes on the isotopic composition ($\delta^{18}$O and $\delta$D) of precipitation and atmospheric water in the tropics: 2. Physical interpretation of the amount effect: Journal of Geophysical Research, v. 113, D19306, http://dx.doi.org/10.1029/2008JD009943

Roeckner, E., Bäuml, G., Bonaventura, L., Brokopf, R., Esch, M., Giorgetta, M., Hagemann, S., Kirchner, I., Kornblueh, L., Manzini, E., Rhodin, A., Schlese, U., Schulzweida, U., and Tompkins, A., 2003, The atmospheric general circulation model ECHAM5. Part I: Model description: Hamburg, Germany, Max-Planck-Institut für Meterologie, MPI-Rep. v. 349, 140 p.

Rowley, D. B., 2007, Stable isotope-based paleoaltimetry: theory and validation: Reviews in Mineralogy and Geochemistry, v. 66, n. 1, p. 23–52, http://dx.doi.org/10.2138/rmg.2007.66.2

Rowley, D. B., and Garzione, C. N., 2007, Stable Isotope-based paleoaltimetry: Annual Review of Earth and Planetary Sciences, v. 35, p. 463–508, http://dx.doi.org/10.1146/annurev.earth.35.031306.140155

Salathé, E. P., Jr., 2006, Influences of a shift in North Pacific storm tracks on western North American precipitation under global warming: Geophysical Research Letters, v. 33, n. 19, L19820, http://dx.doi.org/10.1029/2006GL026882

Salati, E., Dall'Olio, A., Matsui, E., and Gat, J. R., 1979, Recycling of water in the Amazon Basin: An isotopic study: Water Resource Research, v. 15, n. 5, p. 1250–1258, http://dx.doi.org/10.1029/WR015i005p01250

Schmandt, B., and Humphreys, E., 2011, Seismically imaged relict slab from the 55 Ma Siletzia accretion to the northwest United States: Geology, v. 39, n. 2, p. 175–178, http://dx.doi.org/10.1130/G31558.1

Schmidt, G. A., Bigg, G. R., and Rohling, E. J., 1999, Global Seawater Oxygen-18 Database—v1.21, http://data.giss.nasa.gov/o18data/

Sewall, J. O., and Sloan, L. C., 2006, Come a little bit closer: A high-resolution climate study of the early Paleogene Laramide foreland: Geology, v. 34, n. 2, p. 81–84, http://dx.doi.org/10.1130/G22177.1

Sewall, J. O., Sloan, L. C., Huber, M., and Wing, S., 2000, Climate sensitivity to changes in land surface characteristics: Global and Planetary Change, v. 26, n. 4, p. 445–465, http://dx.doi.org/10.1016/S0921-8181(00)00056-4

Sherwood, S. C., and Dessler, A. E., 2001, A model for transport across the tropical tropopause: Journal of the

Atmospheric Sciences, v. 58, p. 765–779, http://dx.doi.org/10.1175/1520-0469(2001)058⟨0765:
AMFTAT⟩2.0.CO;2

Sjostrom, D. J., Hren, M. T., Horton, T. W., Waldbauer, J. R., and Chamberlain, C. P., 2006, Stable isotopic
evidence for a pre-late Miocene elevation gradient in the Great Plains–Rocky Mountain region, *in*
Willett, S. D., Hovius, N., Brandon, M. T., and Fisher, D. M., editors, Tectonics, Climate, and Landscape
Evolution: Geological Society of America Special Paper, v. 398, p. 309–319, http://dx.doi.org/10.1130/
2006.2398(19)

Smoot, J. P., 1983, Depositional sub-environments in an arid closed basin; the Wilkins Peak Member of the
Green River Formation (Eocene), Wyoming, U.S.A: Sedimentology, v. 30, n. 6, p. 801–827, http://
dx.doi.org/10.1111/j.1365-3091.1983.tb00712.x

Werner, M., Langebroek, P. M., Carlsen, T., Herold, M., and Lohmann, G., 2011, Stable water isotopes in the
ECHAM5 general circulation model: Towards high-resolution isotope modeling on a global scale:
Journal of Geophysical Research, v. 116, D15109, http://dx.doi.org/10.1029/2011JD015681

Wilf, P., Wing, S. L., Greenwood, D. R., and Greenwood, C. L., 1998, Using fossil leaves as paleoprecipitation
indicators: An Eocene example: Geology, v. 26, n. 3, p. 203–206, http://dx.doi.org/10.1130/0091-
7613(1998)026⟨0203:UFLAPI⟩2.3.CO;2

Wing, S. L., and Greenwood, D. R., 1993, Fossils and fossil climate: The case for equable continental interiors
in the Eocene: Philosophical Transactions of the Royal Society, B, v. 341, n. 1297, p. 243–252, http://
dx.doi.org/10.1098/rstb.1993.0109

Wolfe, J. A., 1994, Tertiary climatic changes at middle latitudes of western North America: Palaeogeography,
Palaeoclimatology, Palaeoecology, v. 108, n. 3–4, p. 195–205, http://dx.doi.org/10.1016/0031-
0182(94)90233-X

—— 1997, Relations of environmental changes to angiosperm evolution during the late Cretaceous and
Tertiary, *in* Iwasuki, K., and Raven, P. H., editors, Evolution and Diversification of Land Plants: Japan,
Springer, p. 269–290, http://dx.doi.org/10.1007/978-4-431-65918-1_13

Wolfe, J. A., Schorn, H. E., Forest, C. E., and Molnar, P., 1997, Paleobotanical evidence for high altitudes in
Nevada during the Miocene: Science, v. 276, p. 1672–1675, http://dx.doi.org/10.1126/
science.276.5319.1672

Worden, J., Noone, D., Bowman, K., and The Troposheric Emission Spectrometer Science Team and Data
Contributors, 2007, Importance of rain evaporation and continental convection in the tropical water
cycle: Nature, v. 445, p. 528–532, http://dx.doi.org/10.1038/nature05508

Zachos, J. C., Stott, L. D., and Lohmann, K. C., 1994, Evolution of Early Cenozoic marine temperatures:
Paleoceanography, v. 9, n. 2, p. 353–387, http://dx.doi.org/10.1029/93PA03266

Zhou, J., Poulsen, C. J., Pollard, D., and White, T. S., 2008, Simulation of modern and middle Cretaceous
marine $\delta^{18}O$ with an ocean-atmosphere general circulation model: Paleoceanography, v. 23, n. 3,
http://dx.doi.org/10.1029/2008PA001596

Zimmermann, U., Ehhalt, D., and Münnich, K. O., 1967, Soil water movement and evapotranspiration
change in the isotopic composition of the water, *in* IAEA, editors, Isotopes in Hydrology: Vienna,
Austria, Proceedings of the Symposium of Isotopes in Hydrology, p. 567–585.